Constitutive Modelling of Tendons as Fibre-Reinforced Soft Tissues with a Single Fibre Family: Stress-Relaxation Tests for Parameter Identification

applied sciences

MDPI

Article

Constitutive Modelling of Tendons as Fibre-Reinforced Soft Tissues with a Single Fibre Family: Stress-Relaxation Tests for Parameter Identification

Vito Burgio, Martina Di Giacinti, Paola Antonaci and Cecilia Surace *

BIO-MAterials and STructures Laboratory (BIOMAST Lab), Department of Structural, Geotechnical and Building Engineering, Politecnico di Torino, Corso Duca degli Abruzzi 24, 10129 Torino, Italy; vito.burgio@polito.it (V.B.); martina.digiacinti@polito.it (M.D.G.); paola.antonaci@polito.it (P.A.)
* Correspondence: cecilia.surace@polito.it

Featured Application

The work presented here is intended to provide an experimental methodology and the constitutive modelling of porcine FDS tendon as an animal surrogate model for testing traditional repair techniques or new innovative devices for hand tendon repair.

Abstract

Background: Nowadays, flexor hand tendon repair represents a clinical need, and new suture patterns or devices are commonly tested on animal surrogates. Considering the literature, the most frequently adopted animal models for testing are the equivalent tendons taken from porcine specimens. The constitutive modelling of these tendons could open the way to the numerical testing of new repair techniques and the development of digital twins, reducing the use of animal models. Methods: Uniaxial tensile stress-relaxation tests at different strain levels during the loading and unloading phases on porcine tendons were performed. Constitutive formulations based on the assumptions of incompressible and nearly incompressible materials were evaluated. Results: The experimental data were evaluated considering the relaxation tests at different strain levels during both the loading and unloading phases. The experimental tests were used for the material parameter calibration of both models. Conclusions: The stress-relaxation tests conducted at different strain levels during the loading phase showed good agreement with previous findings reported in the literature. Both constitutive model formulations provided a reliable approximation for numerical simulations.

Keywords: constitutive laws; soft tissues modelling; flexor hand tendon repair

Academic Editor: Scott Wood and Arkady Voloshin

Received: 9 October 2025
Revised: 15 December 2025
Accepted: 29 December 2025
Published: 31 December 2025

1. Introduction

Nowadays, tendon injuries represent a considerable economic and social burden for both the healthcare system and patients involved. Tendon repair remains a challenge despite the important advances in biomaterials, surgical techniques, and post-operative rehabilitation protocols. The number of complications and failures is significant, and a secondary surgery is often required. The hand, Achilles, and rotator cuff tendons represent the most common tendon injuries treated by orthopaedic surgeons worldwide. Several studies have reported that the incidence rates of these injuries vary considerably between countries, with an increasing number of cases observed each year [1].

Achilles tendon (AT) ruptures are one of the most commonly treated injuries in the adult population. During a 15-year nationwide study in Italy, the AT rupture incidence rate was 13.1 per 100,000 person-years, implying that more than 118,000 AT repairs were performed in Italy [2].

Traumatic tendon injuries of the hand and wrist are commonly encountered in the emergency department, with an incidence rate of 33.2 injuries per 100,000 person-years in the United States. The highest incidence occurs in young people (20–29 years) [3].

The most commonly injured tendons in the hand are the flexor and extensor tendons of the fingers, and the most common causes of these injuries are penetrating trauma, cut wounds (from knives, glass, etc.), and contusion or abrasion injuries [4,5].

The evaluation of different repair methods and the development of new innovative repair devices or techniques are commonly performed on animal tendons or human cadaveric tendons; human samples in general are difficult to obtain. Furthermore, animal samples are preferred during preclinical phases. In the literature, animal samples are used for two main research purposes: (i) the evaluation of tissue healing through different strategies (for example, after growth factor or stem cell injection) and (ii) suture pattern or device validation.

From a mechanical standpoint, the selection of an appropriate animal tendon that replicates the mechanical properties of the human counterpart is crucial when assessing new devices or surgical techniques [6–9].

Considering hand tendons, in particular the flexor digitorum profundus (FDP) and the flexor digitorum superficialis (FDS), many studies have used equivalent tendons obtained from porcine or chicken specimens. These two species, in fact, have been found to have the greatest similarities with humans. Porcine tendons are widely used due to their comparable size and mechanical behaviour, showing similar stiffness, elongation, and ultimate load values to those of human tendons [10–12].

Experimental tests represent a fundamental step in validating devices or surgical techniques. However, computational methods enable the simulation of different scenarios, accounting for varying physiological or non-physiological loading conditions.

Computational biomechanics, particularly through the finite element method (FEM), provides access to quantities that are difficult to measure in vivo, such as strain and stress distributions, offering a more comprehensive and promising approach to improving devices or surgical techniques [13]. However, developing reliable finite element models of organs and tissues requires accurate constitutive formulations, which necessitate an experimental campaign involving diverse tests on tissues to identify model parameters.

In this work, porcine FDS tendons were tested as surrogates for human FDS hand tendons, providing a mechanical characterisation and evaluation of their visco-hyperelastic properties.

In particular, this work presents the following:

(1) An experimental mechanical protocol, consisting of uniaxial tensile stress-relaxation tests during both the loading and unloading phases;
(2) Two visco-hyperelastic formulations for tendons: the first assumes an incompressible material, while the second considers a nearly incompressible material.

The results of this work represent a starting point for the development of in silico models aimed at validating new devices for hand tendon repair. In silico models of these tendons could facilitate the numerical evaluation of both new and existing repair techniques. The adoption of such models could contribute to a reduction in the use of animal experiments. Furthermore, the development of these models could take into account inter-individual variability, as well as the effects of age and pathological conditions.

The experimental methodology presented provides a standard approach for the calibration of constitutive models for soft tissues, offering a reliable framework for characterising the visco-hyperelastic behaviour of FDS tendons.

This study is closely aligned with ongoing research at the BIOMAST Lab (BIO-Materials and STructures Laboratory) at the Politecnico di Torino. In particular, a new device for hand tendon repair, T-REMEDIE (Tendon Repair MEdical DevIcE) [patent IDs: IT202000006967A1 and WO 2021/198969 A1], has been developed in the laboratory as a novel biocompatible and bioresorbable alternative to sutures.

2. Materials and Methods

2.1. Experimental Tests

All experimental activities were performed at room temperature within 12 h of animal sacrifice. Tendons were measured using a thickness gauge for thickness and width, while a digital calliper was used to measure the initial length (l_0 = grip-to-grip length). Thickness and width were recorded at three different positions along the specimen length. Data on sample geometry (length, width, and thickness) are reported in Tables 1 and 2. For each specimen, the mean cross-sectional area was calculated using the average thickness and width values, assuming an elliptical cross-section. The experimental data are presented by dividing the FDS tendons into two categories: "Thick" and "Thin".

Table 1. Width, thickness, and length in millimetres (mm) of specimens belonging to the "Thick" category.

	Width (mm)			Thickness (mm)			l_0 (mm)
	Distal	**Medial**	**Proximal**	**Distal**	**Medial**	**Proximal**	
Specimen 1	4.92	5.80	6.47	2.93	2.34	2.34	46.63
Specimen 2	4.03	5.24	6.73	2.89	2.78	1.98	38.28
Specimen 3	4.46	3.35	5.37	2.28	2.23	1.65	28.44
Specimen 4	5.25	6.29	7.29	2.63	2.46	2.45	50.90
Specimen 5	4.82	5.22	7.63	2.40	2.61	2.47	50.90
Specimen 6	4.73	5.07	7.16	3.17	2.78	2.99	44.06
Specimen 7	5.14	5.54	6.34	2.72	2.82	2.50	43.53
Specimen 8	4.67	5.19	6.73	2.27	2.07	2.60	57.80
Specimen 9	4.87	5.31	7.63	2.06	2.13	2.73	40.09
Specimen 10	4.29	4.73	6.15	2.45	2.36	2.94	50.12
Mean ± standard deviation	4.72 ± 0.37	5.17 ± 0.77	6.75 ± 0.71	2.58 ± 0.35	2.46 ± 0.28	2.46 ± 0.41	/

The subdivision into "Thick" and "Thin" tendons was introduced purely for descriptive purposes to facilitate the visual presentation of the results. This classification is based exclusively on the measured tendon thickness, and no physiological or biomechanical distinction between such categories has been reported in the literature for porcine FDS tendons.

All tests were performed at room temperature, with the specimens kept well hydrated and under a displacement rate of 10 mm/min. A preconditioning test was carried out by applying ten loading–unloading cycles between 0% and 3% strain for each specimen. The preconditioning protocol was selected based on the authors' previous work, which indicated that preconditioning tests are typically performed using ten to twenty cycles at low strain or force values. However, no standard strain or force values have been reported in the literature [6,7].

Each test consisted of uniaxial tensile stress-relaxation experiments at different strain levels during the loading (3%, 6%, 9%, and 10%) and unloading phases (10%, 9%, and

6%). The loading phase concluded at a maximum strain of 12%, after which the unloading phase began, including three distinct relaxation levels. The final strain level of the loading phase was determined based on preliminary tensile tests, in which sample failure occurred between 13% and 15% strain. The hold time for the relaxation phases was chosen based on typical relaxation times of soft biological tissues reported in the literature, approximately 300 s. Literature reports indicate that this duration allows for the near-complete development of relaxation phenomena [14–16]. The data collected at the end of each relaxation phase enabled the estimation of the equilibrium mechanical behaviour of the specimens, where time-dependent microstructural rearrangements are assumed to be fully developed.

Table 2. Width, thickness, and length in millimetres (mm) of specimens belonging to the "Thin" category.

	Width (mm)			Thickness (mm)			l_0 (mm)
	Distal	Medial	Proximal	Distal	Medial	Proximal	
Specimen 1	4.57	3.69	3.67	1.71	1.43	1.43	38.28
Specimen 2	4.05	3.97	3.96	1.64	1.70	1.78	38.28
Specimen 3	4.00	3.50	3.06	1.53	1.37	1.65	29.44
Specimen 4	4.12	4.37	4.62	1.36	1.24	1.39	50.90
Specimen 5	3.49	4.02	4.49	1.30	1.23	1.36	50.90
Specimen 6	4.38	4.21	4.47	1.39	1.58	1.54	35.84
Specimen 7	5.70	4.29	5.77	1.60	1.39	1.47	44.72
Specimen 8	4.86	3.83	5.26	1.28	1.32	1.62	57.80
Specimen 9	4.38	4.15	4.07	1.45	1.33	1.19	40.86
Specimen 10	4.20	3.94	4.70	1.34	1.14	1.23	45.42
Mean ± standard deviation	4.37 ± 0.59	4.0 ± 0.27	4.41 ± 0.77	1.46 ± 0.15	1.37 ± 0.17	1.46 ± 0.19	/

During the experimental campaign, an unusual behaviour was observed in the unloading phase, specifically in the relaxation segment at 10% strain. To determine whether this behaviour was intrinsic or due to experimental artefacts, three additional tests were performed for each FDS tendon category, adopting a shorter relaxation time of 60 s and including an additional relaxation segment at 12% strain.

All testing was carried out on an MTS Insight® Electromechanical Testing System with a 1000 Newton (N) load cell.

Specimens that exhibited abnormal behaviour (for example, breaking near the machine grips, slippage, or if the authors doubted the validity of the test) were not included in the study. During the entire experimental campaign, 7 specimens were excluded overall due to breaking near the machine grips.

From these data, the total percentage of stress lost (PSL) was calculated for the different relaxation phases [17]. PSL was defined as the difference between the peak engineering stress ($\underline{\boldsymbol{P}}$ = First Piola–Kirchhoff stress tensor or engineering stress) at the beginning of the relaxation phase (T_{in}) and the engineering stress measured at the end of that specific relaxation phase (T_{end}), normalised by the peak engineering stress.

Considering the case of uniaxial tensile test the PSL was calculated using the following formula:

$$PSL = \frac{\left(P_{11}^{Tin} - P_{11}^{Tend}\right)}{P_{11}^{Tin}} \quad (1)$$

Considering a reference system where the longitudinal direction of the tendon is aligned with the x-axis, P_{11} represents the component in the first row and first column of the tensor $\underline{\boldsymbol{P}}$, where the index 1 refers to the x-direction.

2.2. Constitutive Modelling

The fundamental descriptor of the local kinematics is the deformation gradient $\underline{\boldsymbol{F}}$, which is crucial in nonlinear continuum mechanics. The deformation gradient $\underline{\boldsymbol{F}}$ is a tensor that describes the state of deformation of the body, accounting for both stretches and rigid body motions. Considering the case of a general material (or a soft tissue assumed as compressible):

$$J = determinant\left(\underline{\boldsymbol{F}}\right) > 0 \tag{2}$$

Instead, in the case of an incompressible material:

$$J = determinant\left(\underline{\boldsymbol{F}}\right) = 1 \tag{3}$$

When investigating composite soft tissues with one or two fibre families to develop constitutive laws for studying physiological loading conditions using Finite Element Analysis or other methods, the continuum approach is preferred [18]. This is because tissue properties are directly defined by experimental data, unlike other approaches, in which the behaviour of individual constituents is required but often cannot be explicitly determined. The strain energy function Ψ for a soft tissue with one family of fibres is developed considering the contributions originating from the fibres and the matrix. The strain energy function Ψ is expressed as a function of the right Cauchy–Green strain tensor $\underline{\boldsymbol{C}}$.

$$\underline{\boldsymbol{C}} = \underline{\boldsymbol{F}}^T \underline{\boldsymbol{F}} \tag{4}$$

In general, the strain energy function Ψ is divided into two terms, one that describes the matrix contribution and one that describes the fibre contribution. The fibre contribution refers to the mechanical contribution of the collagen fibrils within the tendon.

$$\Psi\left(\boldsymbol{C}\right) = \Psi_{Matrix}\left(\underline{\boldsymbol{C}}\right) + \Psi_{Fibre}\left(\underline{\boldsymbol{C}}, \underline{\boldsymbol{a_0}} \bigotimes \underline{\boldsymbol{a_0}}\right) = \Psi_{Matrix}(I_1, I_2, I_3) + \Psi_{Fibre}(I_4, I_5) \tag{5}$$

The invariants of $\underline{\boldsymbol{C}}$ are defined by the following equations:

$$I_1\left(\underline{\boldsymbol{C}}\right) = trace\left(\underline{\boldsymbol{C}}\right) \tag{6}$$

$$I_2\left(\underline{\boldsymbol{C}}\right) = \frac{1}{2}\left(\left(trace\left(\underline{\boldsymbol{C}}\right)\right)^2 - trace\left(\underline{\boldsymbol{C}}^2\right)\right) \tag{7}$$

$$I_3(\boldsymbol{C}) = \det\left(\underline{\boldsymbol{C}}\right) = J^2 \tag{8}$$

The fibre term is expressed as function of $\underline{\boldsymbol{C}}$ and $\underline{\boldsymbol{a_0}} \otimes \underline{\boldsymbol{a_0}}$. The unit vector $\underline{\boldsymbol{a_0}}$ describes the orientation of the fibre into the reference configuration [19]. The symbol $\otimes$ denotes the dyadic product, and $\underline{\boldsymbol{a_0}} \otimes \underline{\boldsymbol{a_0}}$ represents a structural tensor that describes the fibre architecture inside the tissue. Introducing the structural contribution of the fibres, two pseudo-invariants of $\underline{\boldsymbol{C}}$ and $\underline{\boldsymbol{a_0}} \otimes \underline{\boldsymbol{a_0}}$ are added to the constitutive formulation, and are defined as the following equation:

$$I_4\left(\underline{\boldsymbol{C}}, \underline{\boldsymbol{a_0}} \bigotimes \underline{\boldsymbol{a_0}}\right) = \underline{\boldsymbol{a_0}} \cdot \underline{\boldsymbol{C}}\underline{\boldsymbol{a_0}} = \lambda_{fibre}^2 \tag{9}$$

$$I_5\left(\underline{\boldsymbol{C}}, \underline{\boldsymbol{a_0}} \bigotimes \underline{\boldsymbol{a_0}}\right) = \underline{\boldsymbol{a_0}} \cdot \underline{\boldsymbol{C}}^2\underline{\boldsymbol{a_0}} \tag{10}$$

The two pseudo-invariants I_4 and I_5 describe the properties of the fibres and the fibre–matrix interaction [18].

In particular, I_5 specifies the fibre–matrix contribution to the overall tissue mechanical response, a contribution that becomes experimentally evident when complex strain conditions, such as simple shear, are applied. The relevance of the fibre–matrix shear contribution mainly depends on the fibre–matrix interface strength. In many studies on soft biological tissues, the weakness of the fibre–matrix interface suggests that the fifth invariant can be neglected in the definition of the constitutive model [20]. Based on this evidence, the I_5 is not included in the constitutive formulations.

Considering the contribution of the matrix Ψ_{Matrix}, in soft biological tissue, the high liquid content of the matrix results in an incompressible or nearly incompressible behaviour. The mechanical behaviour of the matrix is assumed to be isotropic. Hence, the anisotropic behaviour of the soft tissue is entirely determined by the presence of the fibres. The strain energy matrix, Ψ_{Matrix}, is decomposed into a volumetric elastic term ($\Psi_{Volumetric\ Matrix}$) and an isochoric elastic term ($\Psi_{Isochoric\ Matrix}$), which describe the material response to changes in volume and shape, respectively.

$$\Psi_{Matrix}(I_1, I_2, I_3) = \Psi_{Volumetric\ Matrix} + \Psi_{\ Isochoric\ Matrix} \tag{11}$$

Many constitutive formulations for tendons and ligaments in the literature omit the I_2 invariant. Following this approach, and to minimise the number of material parameters, I_2 is also omitted in the present work [15,21,22]. Furthermore, the I_2 invariant becomes relevant primarily under biaxial loading conditions [23]. Adopting a formulation that includes I_2 but calibrating the model solely on uniaxial tests would introduce additional constitutive parameters without providing any improvement in the predictive capability of the model.

The volumetric and isochoric part of the matrix will be treated in the following subsections.

Both models implemented are nonlinear transversely isotropic models, and the formulations selected for the matrix and fibre strain energy functions were chosen based on the experimental behaviour of soft tissues reported in the literature. Furthermore, for the fibre term of the strain energy function, these two formulations are among the most commonly adopted in the literature.

2.2.1. Incompressible Case

Considering the soft biological tissue under investigation as an incompressible material, the volumetric contribution of the matrix $\Psi_{Volumetric\ Matrix}$ is generally defined as the following equation:

$$\Psi_{\ Volumetric\ Matrix} = \ -p(J-1) \tag{12}$$

or alternatively

$$\Psi_{Volumetric\ Matrix} = -p(I_3-1)^2 \tag{13}$$

In the literature, both formulations of the volumetric term of the matrix are adopted. In this work, the formulation reported in Equation (12) is used, following the work of Carniel et al. (2013) [15]. In Equations (12) and (13), p represents the hydrostatic pressure and serves as a *Lagrangian multiplier* to ensure incompressibility. The following formulation for the strain energy function of the isochoric part of the matrix and the fibre is adopted:

$$\Psi_{Isochoric\ Matrix} = \left(\frac{C_1}{\alpha_1}\right)\left(e^{(\alpha_1(I_1-1))}-1\right) \tag{14}$$

$$\Psi_{Fibre}(I_4) = \left(\frac{C_4}{\alpha_4^2}\right)\left(e^{(\alpha_4(I_4-1))}-\alpha_4(I_4-1)-1\right) \tag{15}$$

where C_1 and C_4 are related to the stiffness of the matrix and the fibres [MPa], respectively. Instead, α_1 regulates the nonlinearity of the response, and α_4 is related to the initial crimped conformation of collagen fibres [dimensionless].

The First Piola–Kirchhoff stress tensor $\underline{\boldsymbol{P}}$ is defined as follow:

$$\underline{\boldsymbol{P}} = 2\underline{\boldsymbol{F}}\frac{\partial \Psi}{\partial \underline{\boldsymbol{C}}} = \underline{\boldsymbol{P}}_{Volumetric\ Matrix} + \underline{\boldsymbol{P}}_{Isochoric\ Matrix} + \underline{\boldsymbol{P}}_{Fibre} \tag{16}$$

$$\underline{\boldsymbol{P}}_{Volumetric\ Matrix} = -p\underline{\boldsymbol{F}}^{-T} \tag{17}$$

$$\underline{\boldsymbol{P}}_{Isochoric\ Matrix} = C_1 e^{(\alpha_1(I_1-1))}(2\underline{\boldsymbol{F}} - \frac{2}{3}I_1\underline{\boldsymbol{F}}^{-T}) \tag{18}$$

$$\underline{\boldsymbol{P}}_{Fibre}(I_4) = 2\left(\frac{C_4}{\alpha_4}\right)(e^{(\alpha_4(I_4-1))} - 1)\underline{\boldsymbol{F}}(\underline{\boldsymbol{a_0}} \bigotimes \underline{\boldsymbol{a_0}}) \tag{19}$$

2.2.2. Nearly Incompressible Case

The constitutive formulation presented herein is based on the book *Nonlinear Solid Mechanics: A Continuum Approach for Engineering* [18].

Considering the soft biological tissue under investigation as a nearly incompressible material, a multiplicative decomposition of $\underline{\boldsymbol{F}}$ into a volume-changing $(J^{\frac{1}{3}}\underline{\boldsymbol{I}})$ (dilatational) and volume-preserving $\underline{\boldsymbol{F}}^*$ (distortional) part is adopted. In nearly incompressible materials, dilatational changes require a much higher external work than a volume-preserving changes.

$$\underline{\boldsymbol{F}} = (J^{\frac{1}{3}}\underline{\boldsymbol{I}})\underline{\boldsymbol{F}}^* \tag{20}$$

$$\underline{\boldsymbol{C}} = (J^{\frac{2}{3}}\underline{\boldsymbol{I}})\underline{\boldsymbol{C}}^* \tag{21}$$

where $\underline{\boldsymbol{I}}$ is the identity tensor and $\underline{\boldsymbol{C}}^*$ is the distortional part of $\underline{\boldsymbol{C}}$. The strain energy function for a nearly incompressible material with one fibre family is defined as follows:

$$\Psi\left(\underline{\boldsymbol{C}}^*, \underline{\boldsymbol{a_0}} \bigotimes \underline{\boldsymbol{a_0}}\right) = \Psi_{\substack{Volumetric \\ Matrix}}(J) + \Psi_{\substack{Isochoric \\ Matrix}}(I_1^*, I_2^*) + \Psi_{Fibre}(I_4^*) \tag{22}$$

$$\Psi_{\substack{Volumetric \\ Matrix}}(J) = \frac{K}{2}(J-1)^2 \tag{23}$$

$$\Psi_{Isochoric\ Matrix}(I_1^*) = \left(\frac{C_1}{\alpha_1}\right)(e^{(\alpha_1(I_1^*-1))} - 1) \tag{24}$$

$$\Psi_{Fibre}(I_4^*) = \left(\frac{C_4}{2\alpha_4}\right)(e^{(\alpha_4(I_4^*-1)^2)} - 1) \tag{25}$$

where K is the bulk modulus, Equation (24) coincides with Equation (14), and Equation (25) represents an alternative formulation for describing the strain energy associated with the fibre mechanical behaviour [24,25]. For the same reasons discussed in the previous subsection, the modified invariant I_2^* is also omitted. In Equations (24) and (25), $I_1^* = J^{-\frac{2}{3}}I_1$ and $I_4^* = J^{-\frac{2}{3}}I_4$ are the first and fourth modifier invariants. Then, the First Piola–Kirchhoff stress tensor $\underline{\boldsymbol{P}}$ is defined as follows:

$$\underline{\boldsymbol{P}} = \underline{\boldsymbol{P}}_{Volumetric\ Matrix} + \underline{\boldsymbol{P}}_{Isochoric\ Matrix} + \underline{\boldsymbol{P}}_{Fibre} \tag{26}$$

$$\underline{\boldsymbol{P}}_{Volumetric\ Matrix} = Jp\underline{\boldsymbol{F}}^{-T} \tag{27}$$

$$p = \frac{\partial \Psi_{Volumetric\ Matrix}(J)}{\partial J} = K(J-1) \tag{28}$$

$$\underline{\boldsymbol{P}}_{Isochoric\ Matrix}(I_1^*) = J^{-\frac{2}{3}} C_1 e^{(\alpha_1(I_1^*-1))}(2\underline{\boldsymbol{F}} - \frac{2}{3} I_1 \underline{\boldsymbol{F}}^{-T}) \tag{29}$$

$$\underline{\boldsymbol{P}}_{Fibre}(I_4^*) = J^{-\frac{2}{3}} C_4 (I_4^* - 1)(e^{(\alpha_4(I_4^*-1)^2)} - 1)\left(2\underline{\boldsymbol{F}}\left(\underline{\boldsymbol{a_0}} \bigotimes \underline{\boldsymbol{a_0}}\right) - \frac{2}{3} I_4 \underline{\boldsymbol{F}}^{-T}\right) \tag{30}$$

2.3. Evolution Equations for the Visco-Hyperelasticity Modelling

Soft biological tissues, as well as polymers and other materials, exhibit a time-dependent behaviour. To characterise the viscous process, it is necessary to define an evolution law. When the viscous response of a soft tissue is under investigation, the experimental programme is designed to characterise the instantaneous stress response $\underline{\boldsymbol{P}}^0$ or the equilibrium stress response $\underline{\boldsymbol{P}}^\infty$. The characterisation of $\underline{\boldsymbol{P}}^0$ is carried out using a very high displacement or strain rate; however, this procedure is not widely adopted in the literature. In contrast, the characterisation of $\underline{\boldsymbol{P}}^\infty$ is widely employed, relying on standard displacement or strain rates and a series of stress-relaxation tests conducted at different strain levels.

In particular, two main formulations of the viscous evolution process have been reported in the literature, which are extensions of the generalised Maxwell model for small strain. Both models are based on a mechanical representation comprising an equilibrium branch and viscoelastic branches connected in parallel. Each viscoelastic branch phenomenologically represents a viscoelastic process.

The first viscous formulation is based on the following evolution law:

$$\dot{\boldsymbol{q}}^i + \frac{1}{\tau^i} = \frac{\gamma^i}{\gamma^\infty \tau^i} \underline{\boldsymbol{P}}^\infty \tag{31}$$

where γ^i is the relative stiffness, which is non-dimensional, and τ^i is the relaxation time of the ith branch. The equilibrium spring, characterised by γ^∞, represents the material response when the thermodynamic equilibrium conditions are reached, that is, when all viscous phenomena have been completed [15]. The relative stiffness values should satisfy the following relationship:

$$\gamma^\infty = 1 - \sum_{i=1}^{n} \gamma^i \tag{32}$$

where n represents the number of viscous processes, or networks, considered in the formulation adopted. In the present study, four viscous processes were considered for both the matrix and the fibres.

The second viscous formulation is based on the following evolutionary law:

$$\dot{\boldsymbol{q}}^i + \frac{1}{\tau_i} = \beta_i^\infty \underline{\boldsymbol{P}}^\infty \tag{33}$$

where β_i^∞ is a free-energy factor, which is non-dimensional, positive definite, and describes the rate of decay of the viscoelastic process. Each β_i^∞ is coupled with a relaxation time τ_i [18].

2.4. Constitutive Parameters Calibration

The constitutive parameters were identified by fitting the analytical models to the experimental uniaxial data through a Genetic Algorithm (GA), which efficiently explored the parameter space to minimise the fitting error. A dedicated MATLAB R2022a script was developed for each constitutive formulation, representing the analytical model used to interpret the experimental tests while accounting for the corresponding boundary conditions. In the case of the incompressible material formulation, the deformation gradient $\underline{\boldsymbol{F}}$ is defined as follows:

$$\underline{\boldsymbol{F}} = \begin{bmatrix} \lambda_{11} & 0 & 0 \\ 0 & \frac{1}{\sqrt{\lambda_{11}}} & 0 \\ 0 & 0 & \frac{1}{\sqrt{\lambda_{11}}} \end{bmatrix} \tag{34}$$

where λ_{11} is the stretch ratio in the uniaxial traction direction. The structure of $\underline{\boldsymbol{F}}$ reported in Equation (34) ensures that $J = 1$.

Instead, for a compressible material, the deformation gradient $\underline{\boldsymbol{F}}$ has the following components:

$$\underline{\boldsymbol{F}} = \begin{bmatrix} \lambda_{11} & 0 & 0 \\ 0 & \lambda_{22} & 0 \\ 0 & 0 & \lambda_{33} \end{bmatrix} \tag{35}$$

where λ_{11} is the stretch ratio in the uniaxial traction direction, and λ_{22} and λ_{33} are the stretch ratios along the other two planar directions. Considering the isotropy of the matrix tissue, $\lambda_{22} = \lambda_{33}$.

To calibrate both visco-hyperelastic formulations, the equilibrium stress response $\underline{\boldsymbol{P}}^{\infty}$ was determined using the experimental stress values at the end of each relaxation phase, which enabled the estimation of the equilibrium mechanical behaviour of the specimens, where time-dependent microstructural rearrangements were considered to be completed. Subsequently, after estimating the constitutive parameters describing the equilibrium response, all the experimental stress values collected during the loading phase were used to identify the material parameters governing the viscous behaviour.

The determination of the material parameters was carried out using the following equation:

$$\sum_{i=1}^{N} 100 \cdot \left(1 - \frac{P^{N}_{11\ model}}{P^{N}_{11\ experimental}}\right) \tag{36}$$

where N is the total number of data points collected during the uniaxial tensile stress-relaxation test. Equation (36) provides a normalised point-to-point difference between the experimental and numerical predictions, ensuring accurate calibration results.

3. Results

3.1. Stress-Relaxation Tests

Figures 1–4 present the results of the uniaxial tensile stress-relaxation tests performed at different strain levels during the loading and unloading phases. In particular, Figures 1 and 3 refer to a relaxation time of 300 s, while Figures 2 and 4 show the corresponding tests with a relaxation time of 60 s.

The experimental data showed high variability in the results for the FDS tendons.

In the experimental tests where no stress-relaxation phase was performed at 12% strain, a decrease in strain led to a reduction in tissue relaxation, resulting in a smaller PSL value compared with the other relaxation levels. Conversely, in the experimental tests including a relaxation phase at 12% strain, tendon relaxation increased, and consequently, the PSL parameter exhibited a higher value than at the other levels.

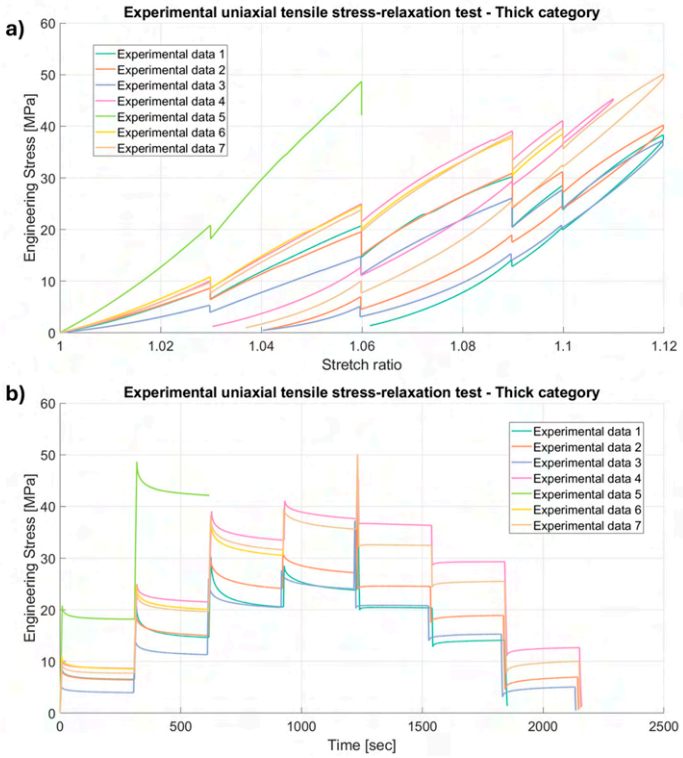

Figure 1. Results of the experimental uniaxial tensile stress-relaxation tests on porcine FDS tendons classified in the "Thick" category, with a relaxation time of 300 s, (**a**) Stretch ratio vs. Engineering Stress and (**b**) Time vs. Engineering Stress.

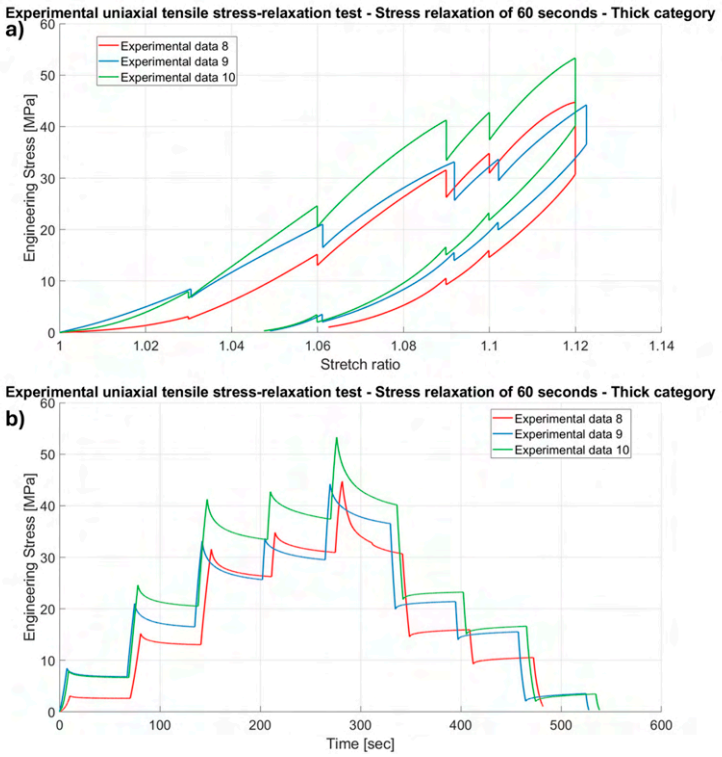

Figure 2. Results of the experimental uniaxial tensile stress-relaxation tests on porcine FDS tendons classified in the "Thick" category, with a relaxation time of 60 s, (**a**) Stretch ratio vs. Engineering Stress and (**b**) Time vs. Engineering Stress.

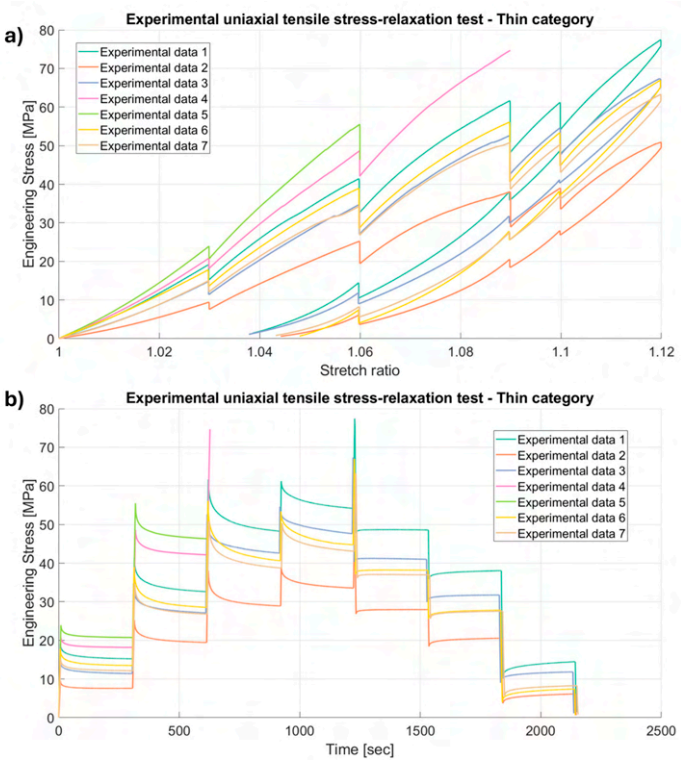

Figure 3. Results of the experimental uniaxial tensile stress-relaxation tests on porcine FDS tendons classified in the "Thin" category, with a relaxation time of 300 s, (**a**) Stretch ratio vs. Engineering Stress and (**b**) Time vs. Engineering Stress.

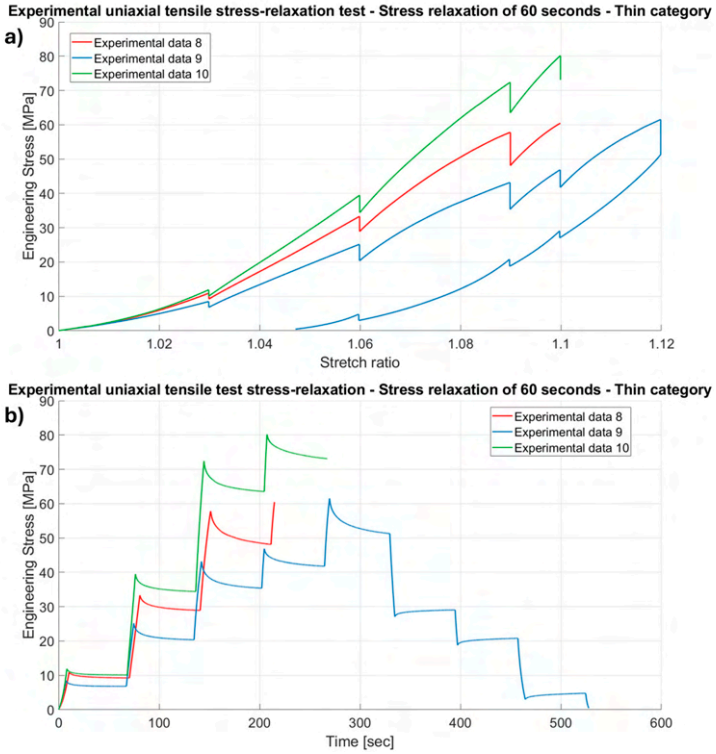

Figure 4. Results of the experimental uniaxial tensile stress-relaxation tests on porcine FDS tendons classified in the "Thin" category, with a relaxation time of 60 s, (**a**) Stretch ratio vs. Engineering Stress and (**b**) Time vs. Engineering Stress.

When comparing the PSL values obtained from experiments with relaxation periods of 300 s and 60 s (see Tables 3 and 4) during the loading phase, the values recorded at 60 s were generally consistent and smaller than those calculated at 300 s.

Table 3. Evaluation of the PSL parameter for FDS tendons classified in the "Thick" category.

	Loading Phase					**Unloading Phase**		
	3%	**6%**	**9%**	**10%**		**10%**	**9%**	**6%**
Specimen 1	22.32	27.40	30.21	15.91		1.44	8.93	/
Specimen 2	23.63	21.46	20.60	12.33		1.45	7.07	46.69
Specimen 3	23.39	21.34	19.53	11.99		1.59	8.24	63.22
Specimen 4	13.11	12.91	18.86	8.13		/	/	/
Specimen 5	11.53	12.42	/	/		/	/	/
Specimen 6	19.57	17.31	17.79	/		/	/	/
Specimen 7	18.93	16.16	16.29	9.81		0.64	4.81	25.22
Mean ± standard deviation	18.93 ± 4.86	18.43 ± 5.34	19.64 ± 5.76	11.63 ± 2.94		1.28 ± 0.43	7.26 ± 1.80	45.04 ± 19.05
	Loading phase					**Unloading phase**		
	3%	**6%**	**9%**	**10%**	**12%**	**10%**	**9%**	**6%**
Specimen 8	15.23	14.08	16.73	11.10	31.21	9.09	13.44	/
Specimen 9	19.20	21.30	22.30	12.30	17.17	7.18	11.00	71.08
Specimen 10	16.22	16.56	18.87	12.52	24.49	6.45	10.32	70.28
Mean ± standard deviation	16.88 ± 2.06	17.31 ± 3.67	19.30 ± 2.81	11.97 ± 0.76	24.29 ± 7.02	7.58 ± 1.36	11.59 ± 1.64	70.68 ± 0.56

Table 4. Evaluation of the PSL parameter for FDS tendons classified in the "Thin" category.

	Loading Phase					**Unloading Phase**		
	3%	**6%**	**9%**	**10%**		**10%**	**9%**	**6%**
Specimen 1	18.95	19.59	20.34	10.89		1.14	5.69	33.22
Specimen 2	17.31	20.88	21.83	12.99		2.98	10.28	57.47
Specimen 3	20.59	19.88	16.99	11.87		0.85	5.24	24.13
Specimen 4	11.53	12.42	/	/		/	/	/
Specimen 5	12.07	15.10	/	/		/	/	/
Specimen 6	22.19	24.44	25.75	15.24		1.95	7.92	70.71
Specimen 7	17.70	20.32	22.17	13.63		1.76	6.72	41.49
Mean ± standard deviation	17.19 ± 4.04	18.93 ± 3.96	21.42 ± 3.17	12.92 ± 1.66		1.73 ± 0.83	7.17 ± 2.02	45.40 ± 18.73
	Loading phase					**Unloading phase**		
	3%	**6%**	**9%**	**10%**	**12%**	**10%**	**9%**	**6%**
Specimen 8	15.24	13.11	16.99	10.51	/	/	/	/
Specimen 9	19.76	18.88	16.60	10.80	16.42	7.06	10.75	59.38
Specimen 10	14.97	12.72	17.84	8.81	/	/	/	/
Mean ± standard deviation	16.67 ± 2.68	14.91 ± 3.44	15.54 ± 2.98	10.04 ± 1.07	16.42 ± 0.0	7.06 ± 0.00	10.76 ± 0.00	59.38 ± 0.00

Considering the relaxation phases during unloading, the PSL parameter increased as the strain level decreased, and the data obtained with a relaxation phase at 12% strain showed higher PSL values.

3.1.1. Evaluation of the Relaxation at Different Strain Levels—Loading

The relaxation processes of each FDS tendon were analysed by normalising the data with respect to the initial value of the corresponding relaxation segment. The normalised relaxation segments are presented in Figures 5–12. Specifically, Figures 5, 6, 9 and 10 compare the same relaxation segment across different tendons, while Figures 7, 8, 11 and 12 show the different normalised relaxation segments within the same tendon. The relaxation segment obtained at 10% strain exhibited a similar behaviour across all specimens.

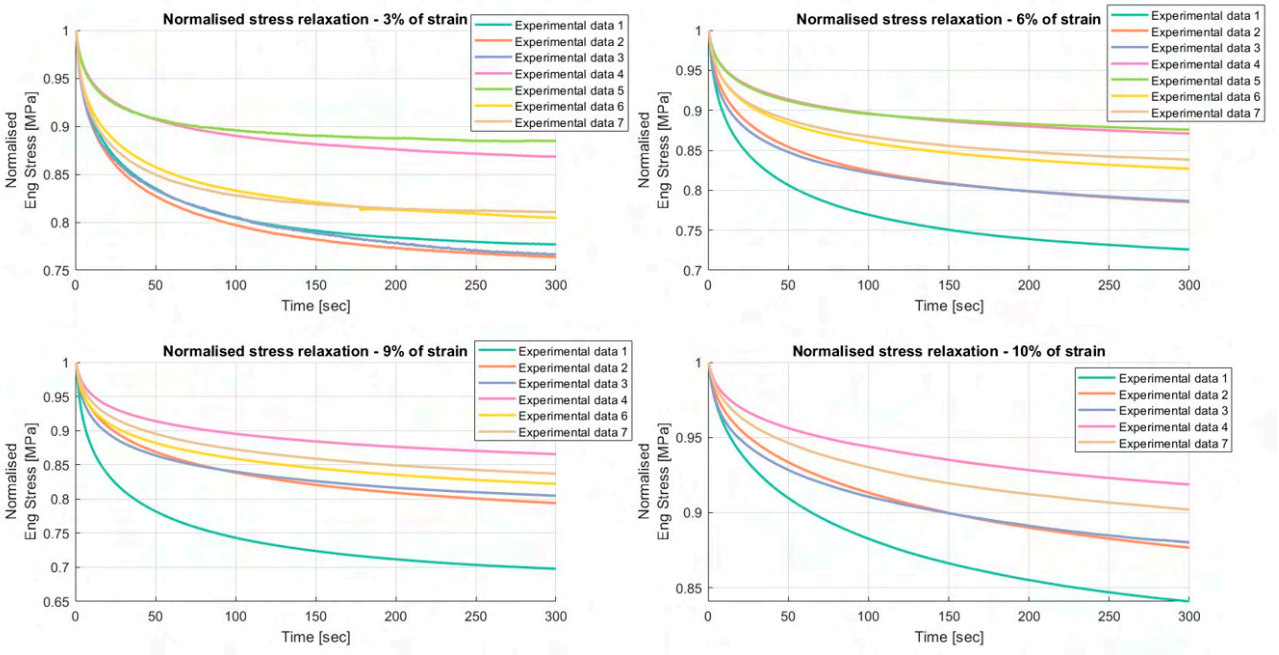

Figure 5. Results of the relaxation segments, during the loading phase, on porcine FDS tendons classified in the "Thick" category, with a relaxation time of 300 s. In each graph, the same normalised relaxation segment for all specimens is reported.

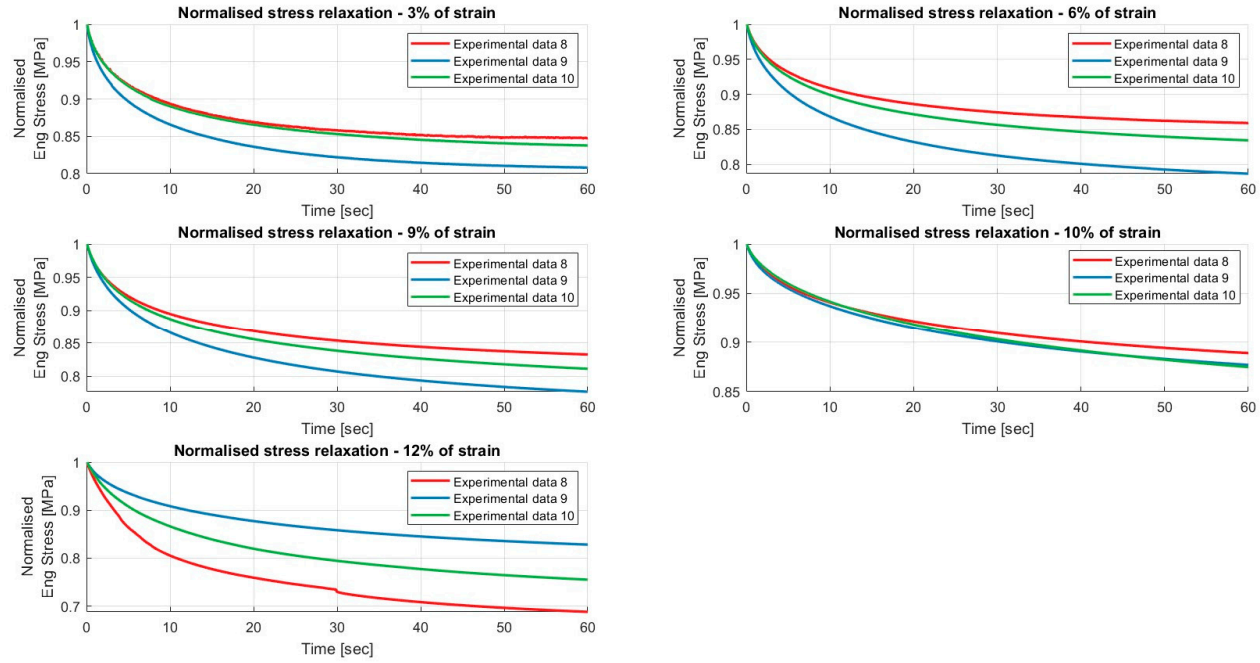

Figure 6. Results of the relaxation segments, during the loading phase, on porcine FDS tendons classified in the "Thick" category, with a relaxation time of 60 s. In each graph, the same normalised relaxation segment for all specimens is reported.

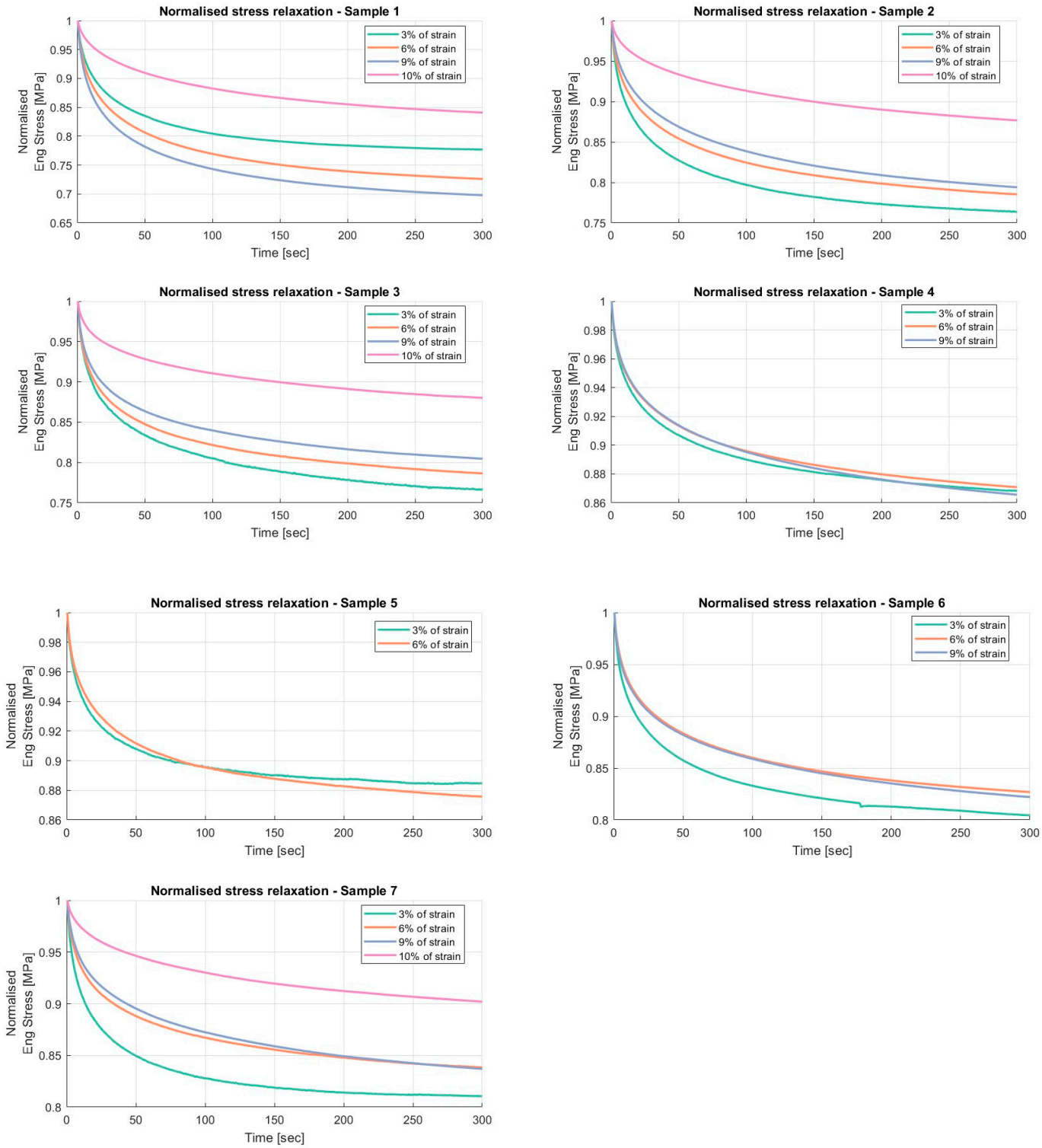

Figure 7. Results of the relaxation segments, during the loading phase, on porcine FDS tendons classified in the "Thick" category, with a relaxation time of 300 s. In each graph, all the normalised relaxation segments for the same specimen are reported.

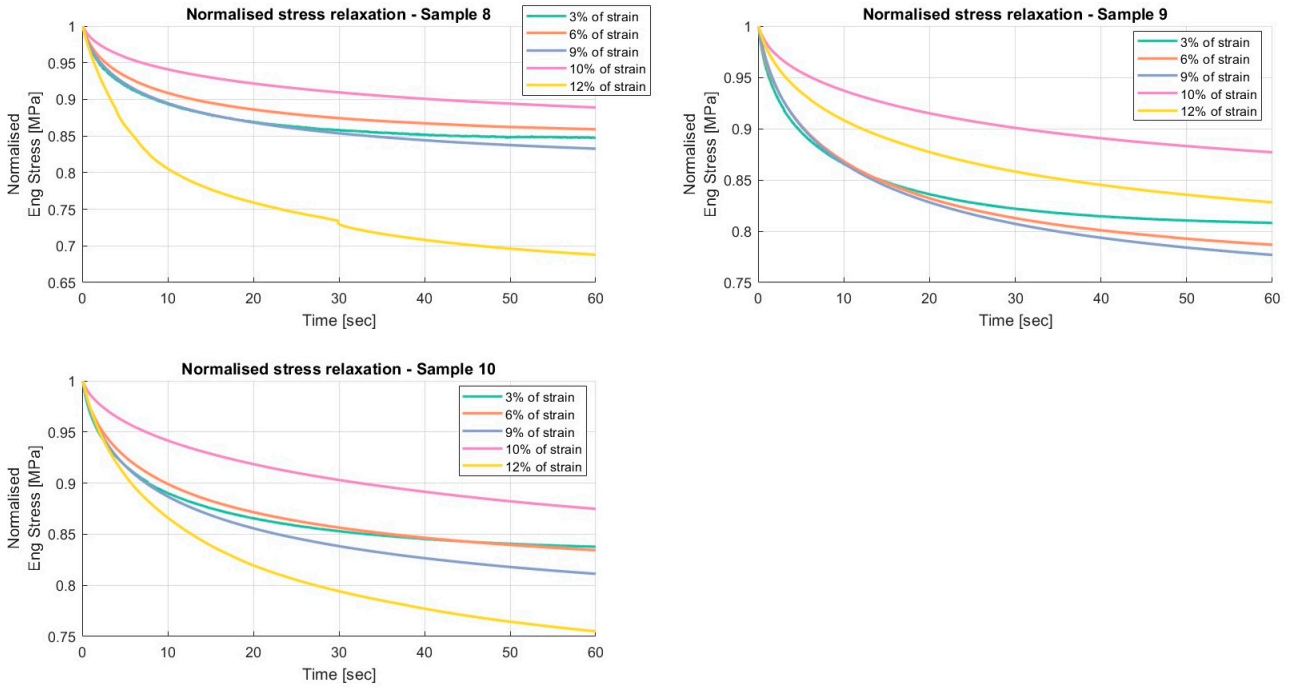

Figure 8. Results of the relaxation segments, during the loading phase, on porcine FDS tendons classified in the "Thick" category, with a relaxation time of 60 s. In each graph, all the normalised relaxation segments for the same specimen are reported.

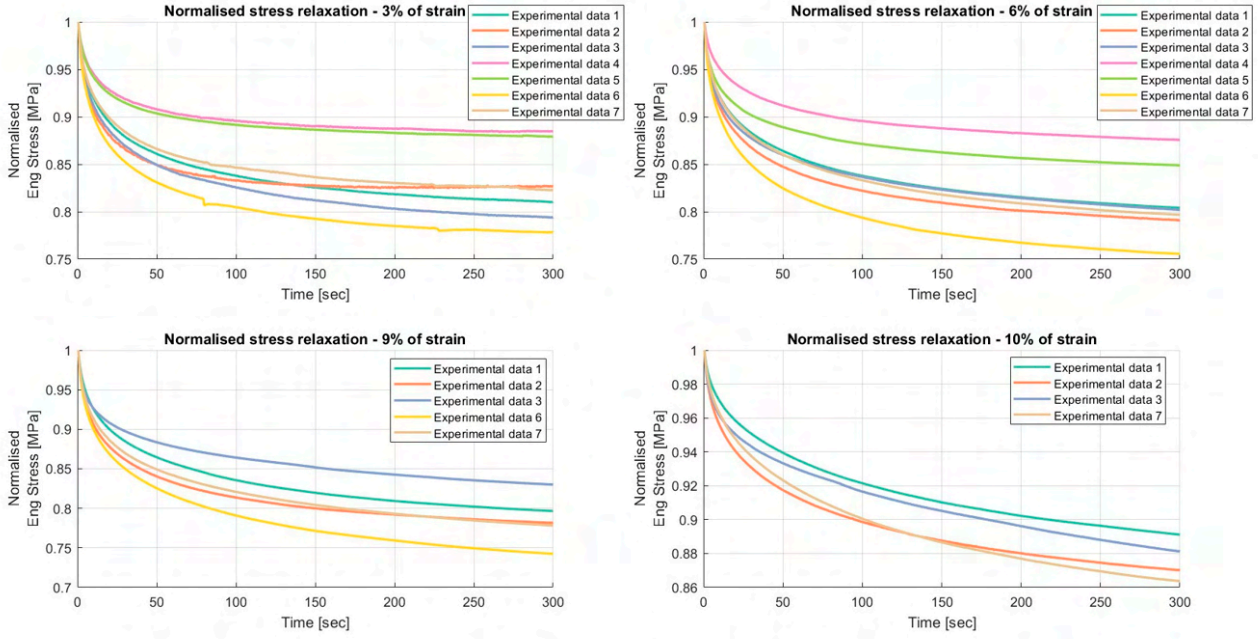

Figure 9. Results of the relaxation segments, during the loading phase, on porcine FDS tendons classified in the "Thin" category, with a relaxation time of 300 s. In each graph, the same normalised relaxation segment for all specimens is reported.

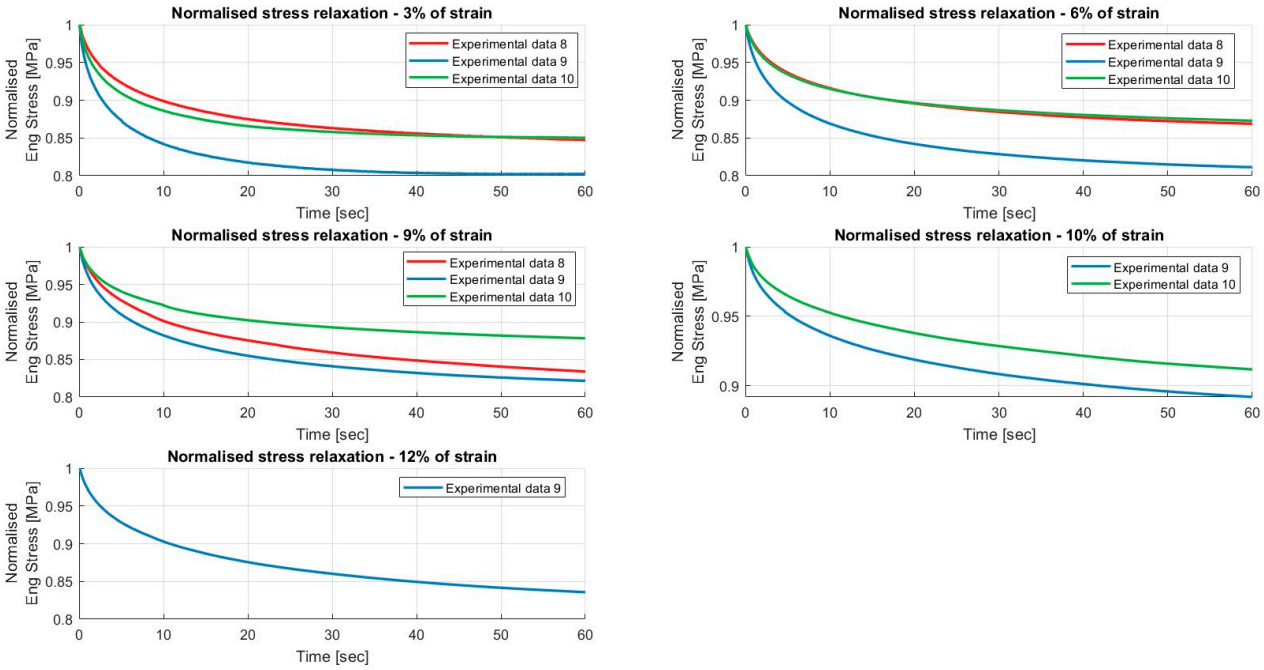

Figure 10. Results of the relaxation segments, during the loading phase, on porcine FDS tendons classified in the "Thin" category, with a relaxation time of 60 s. In each graph, the same normalised relaxation segment for all specimens is reported.

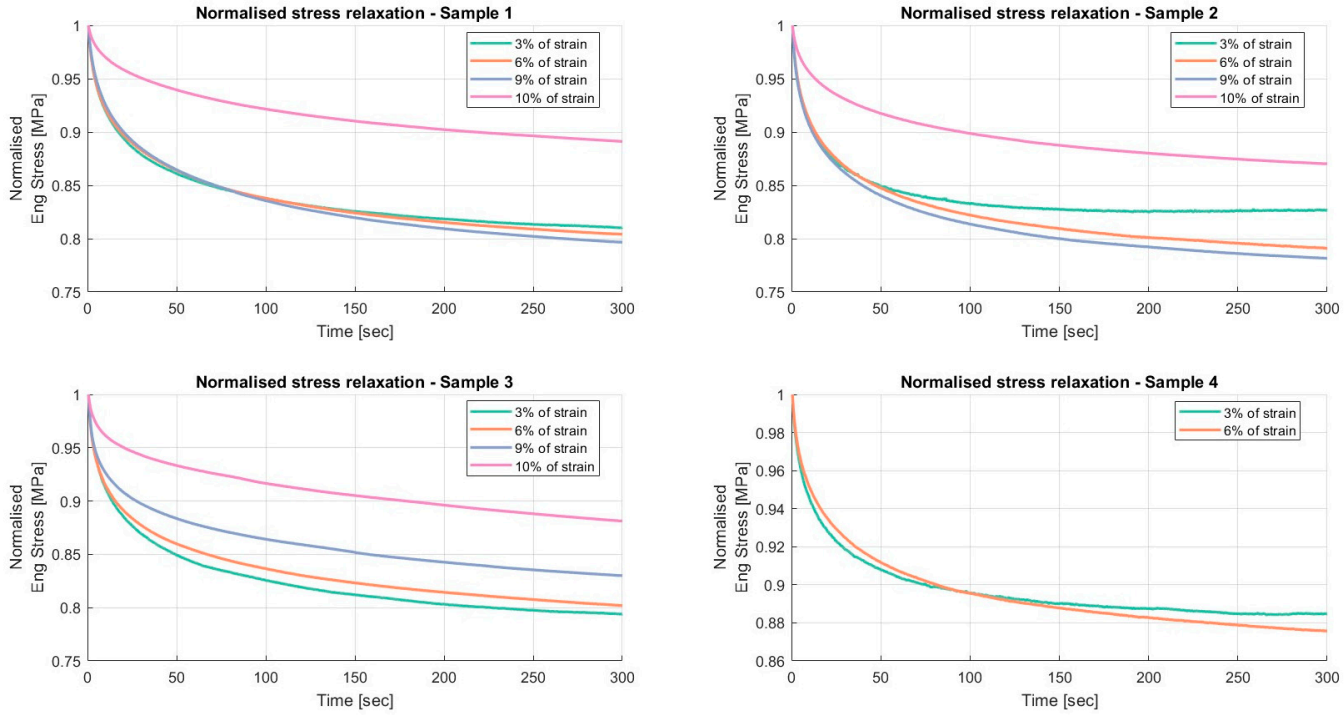

Figure 11. *Cont.*

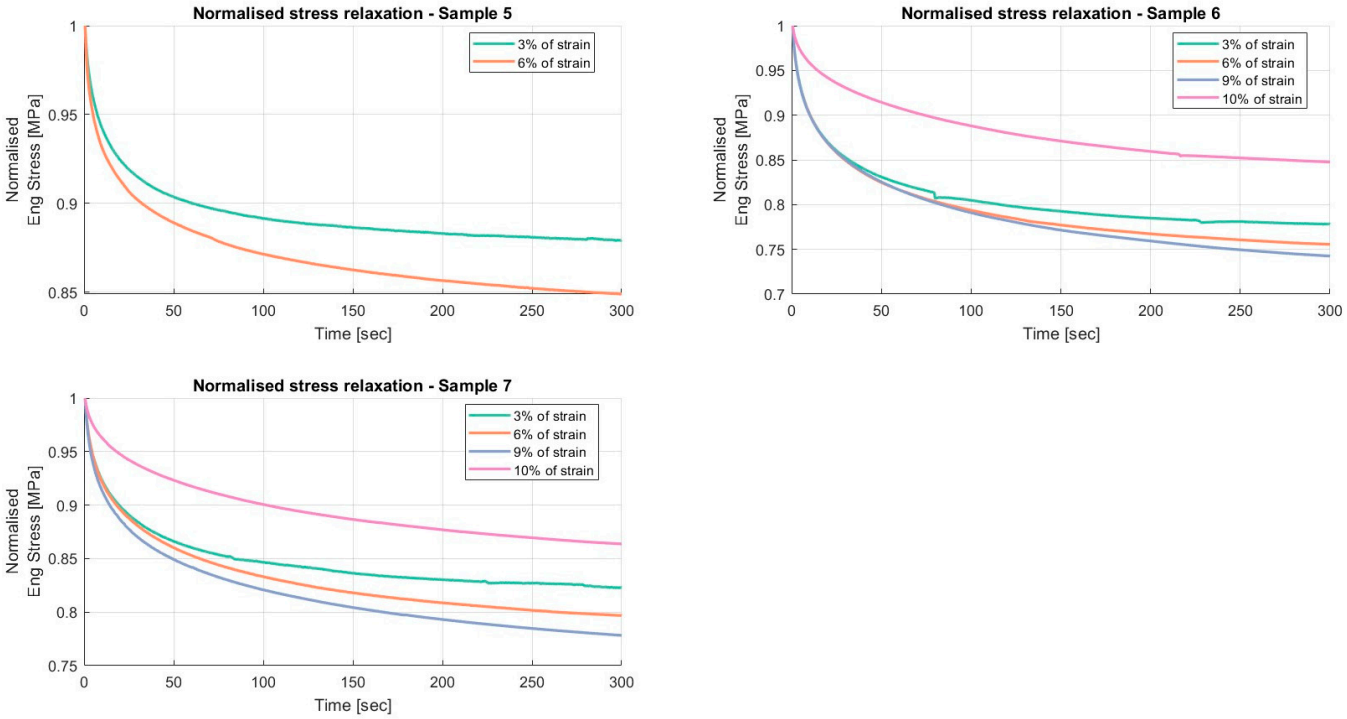

Figure 11. Results of the relaxation segments, during the loading phase, on porcine FDS tendons classified in the "Thin" category, with a relaxation time of 300 s. In each graph, all the normalised relaxation segments for the same specimen are reported.

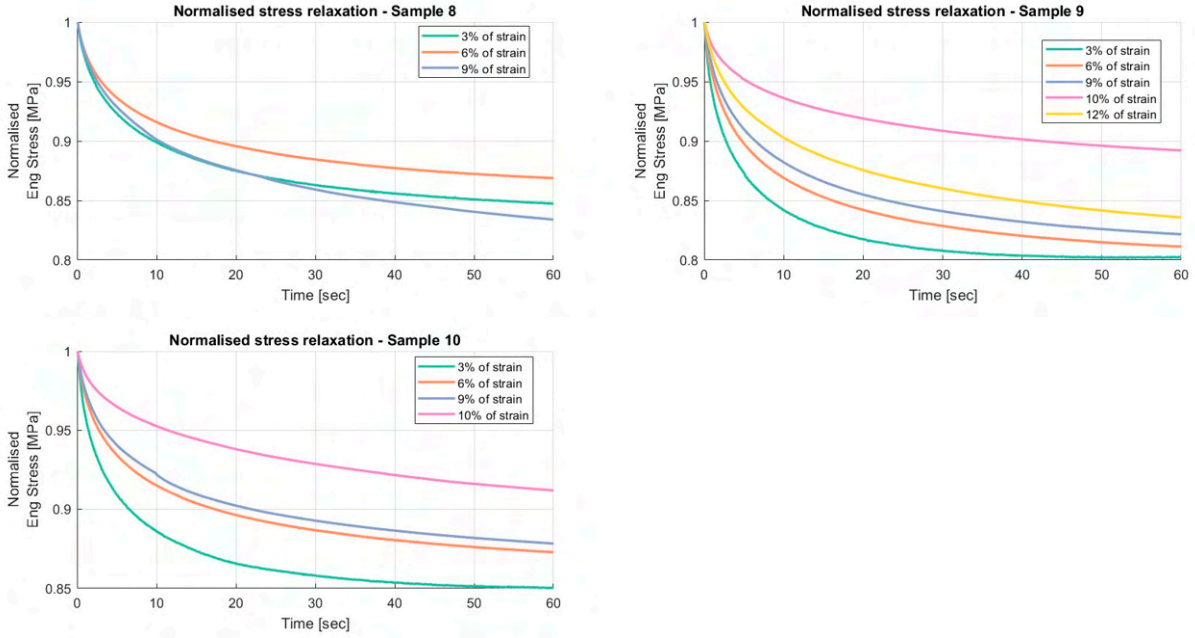

Figure 12. Results of the relaxation segments, during the loading phase, on porcine FDS tendons classified in the "Thin" category, with a relaxation time of 60 s. In each graph, all the normalised relaxation segments for the same specimen are reported.

3.1.2. Evaluation of the Relaxation at Different Strain Levels—Unloading

The relaxation processes of each FDS tendon were analysed by normalising the data with respect to the initial value of the corresponding relaxation segment. The normalised relaxation segments are presented in Figures 13–20. Specifically, Figures 13, 14, 17 and 18 compare the

same relaxation segment across different tendons, while Figures 15, 16, 19 and 20 show the different normalised relaxation segments within the same tendon.

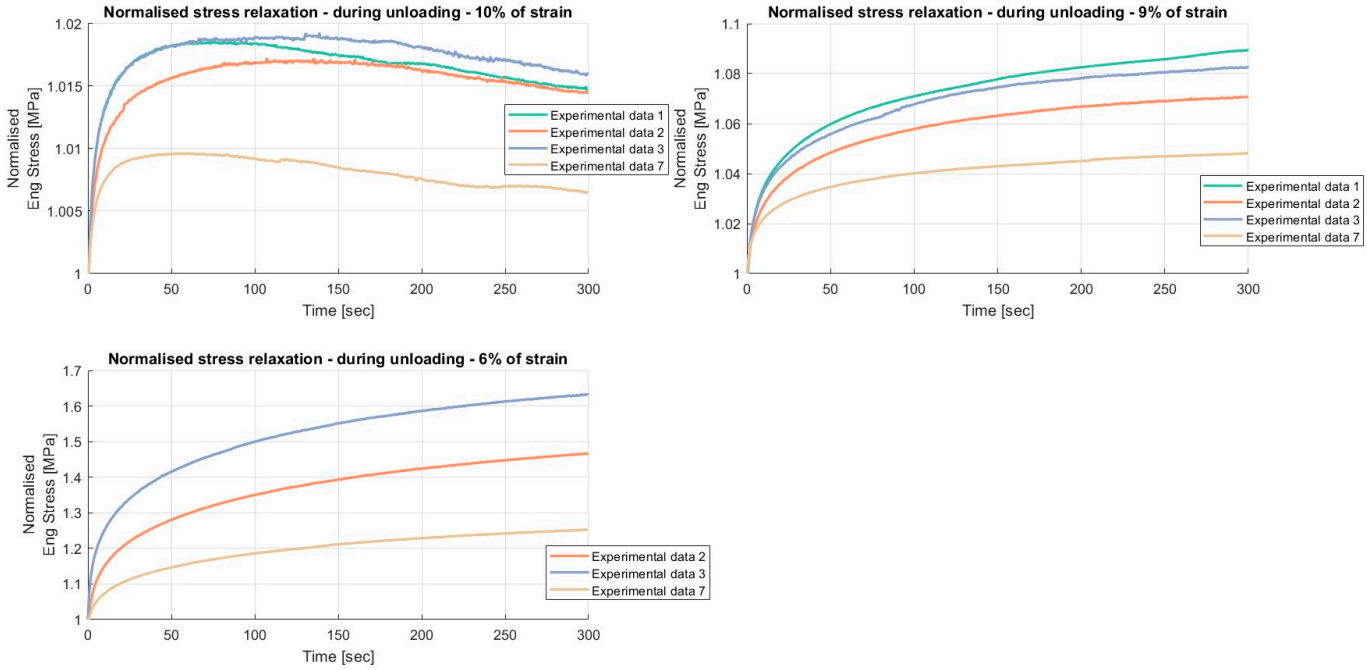

Figure 13. Results of the relaxation segments, during the unloading phase, on porcine FDS tendons classified in the "Thick" category, with a relaxation time of 300 s. In each graph, the same normalised relaxation segment for all specimens is reported.

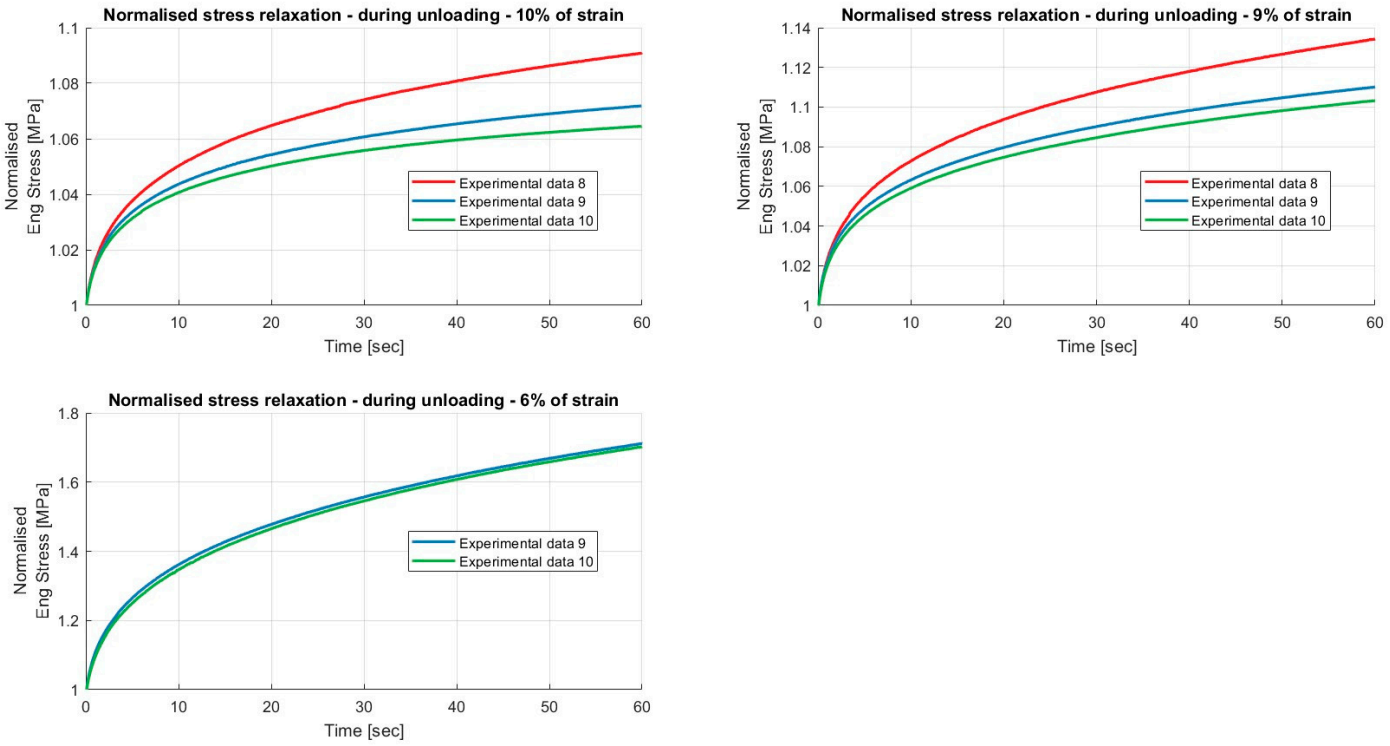

Figure 14. Results of the relaxation segments, during the unloading phase, on porcine FDS tendons classified in the "Thick" category, with a relaxation time of 60 s. In each graph, the same normalised relaxation segment for all specimens is reported.

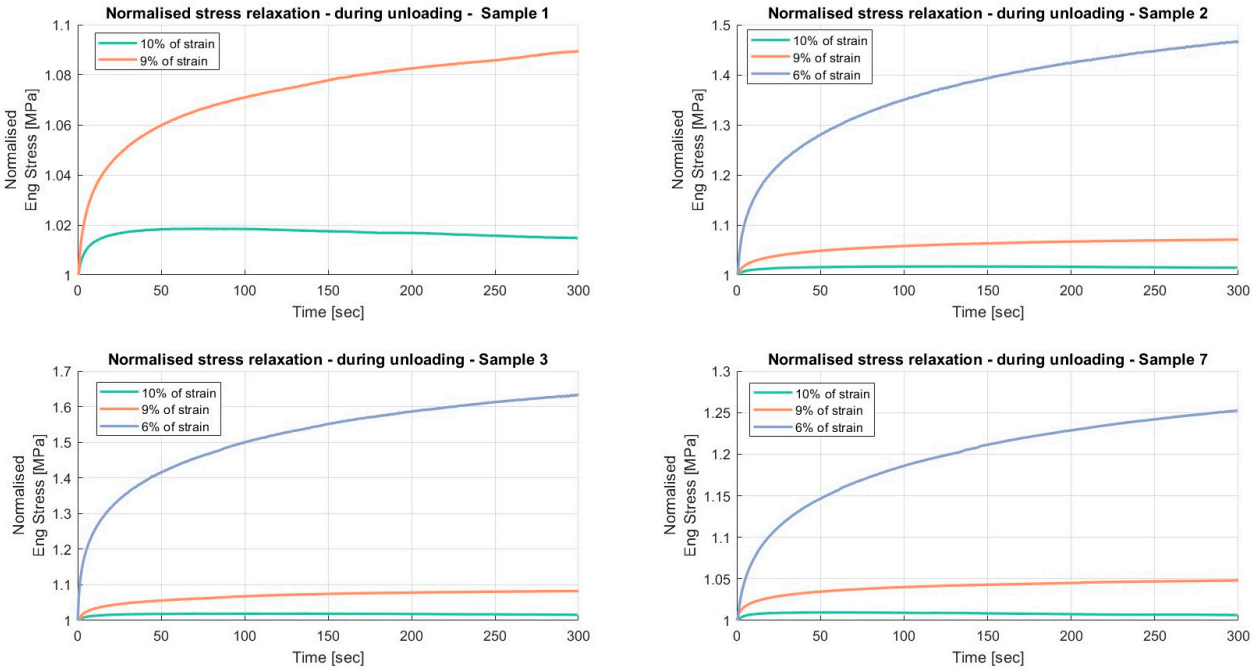

Figure 15. Results of the relaxation segments, during the unloading phase, on porcine FDS tendons classified in the "Thick" category, with a relaxation time of 300 s. In each graph, all the normalised relaxation segments for the same specimen are reported.

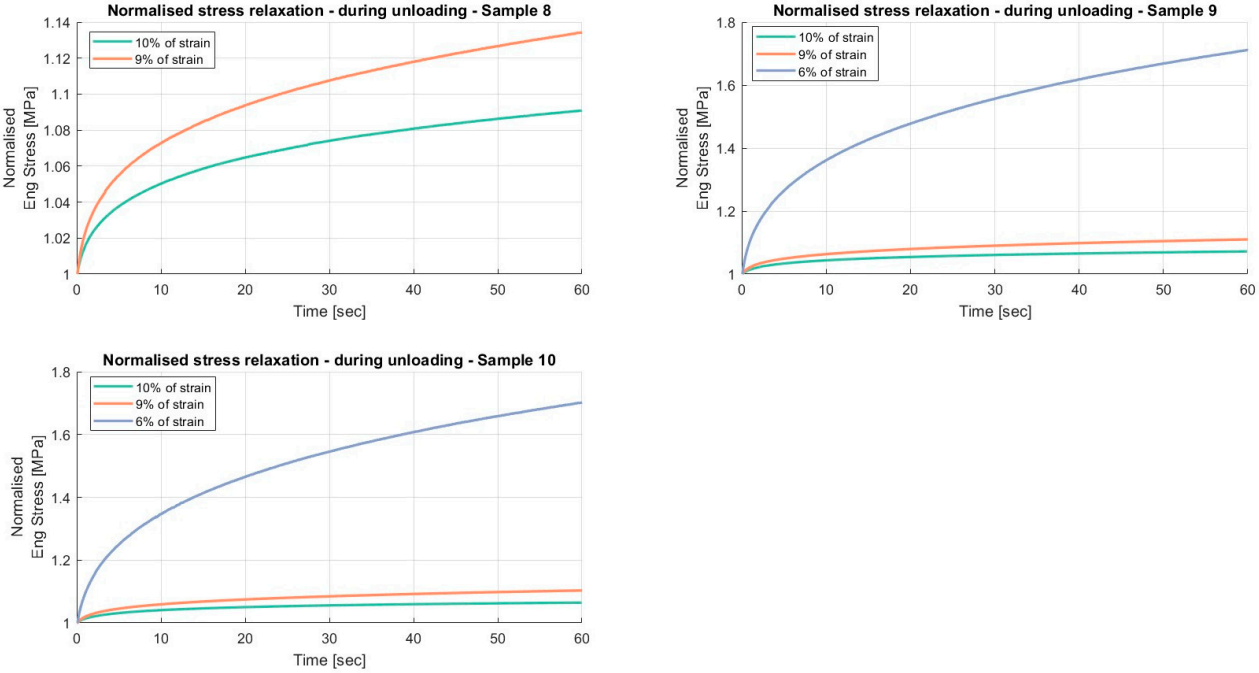

Figure 16. Results of the relaxation segments, during the unloading phase, on porcine FDS tendons classified in the "Thick" category, with a relaxation time of 60 s. In each graph, all the normalised relaxation segments for the same specimen are reported.

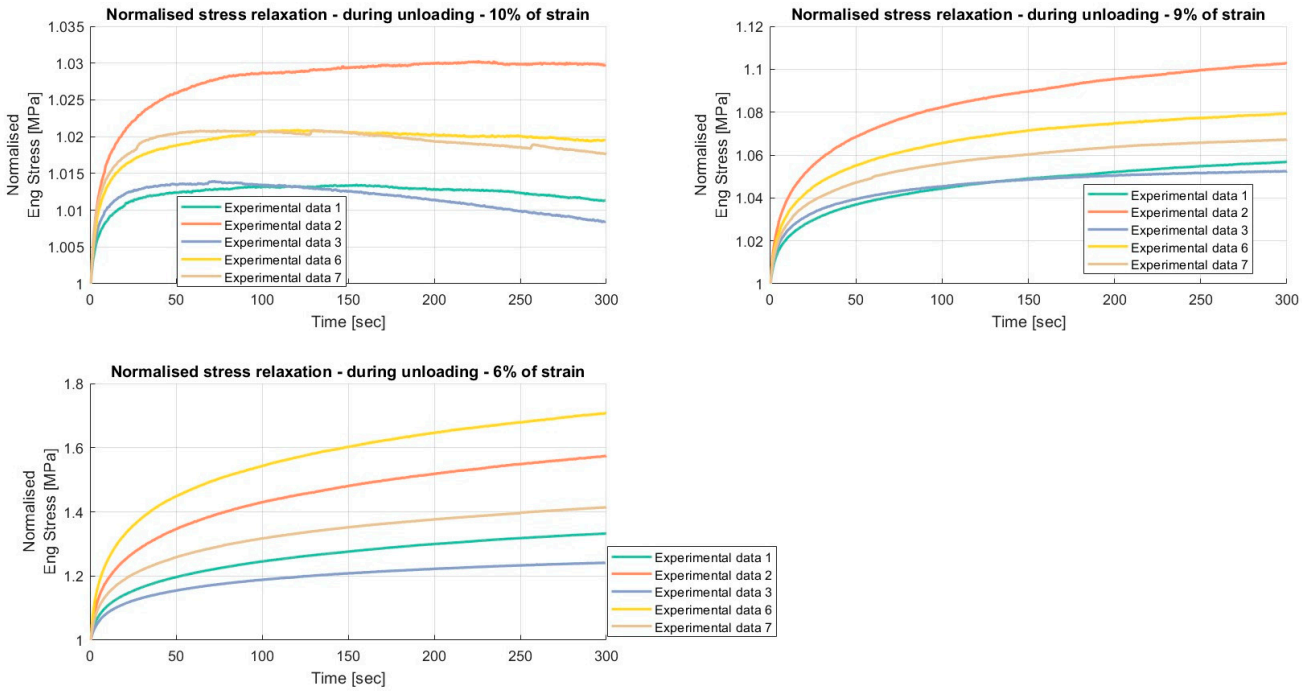

Figure 17. Results of the relaxation segments, during the unloading phase, on porcine FDS tendons classified in the "Thin" category, with a relaxation time of 300 s. In each graph, the same normalised relaxation segment for all specimens is reported.

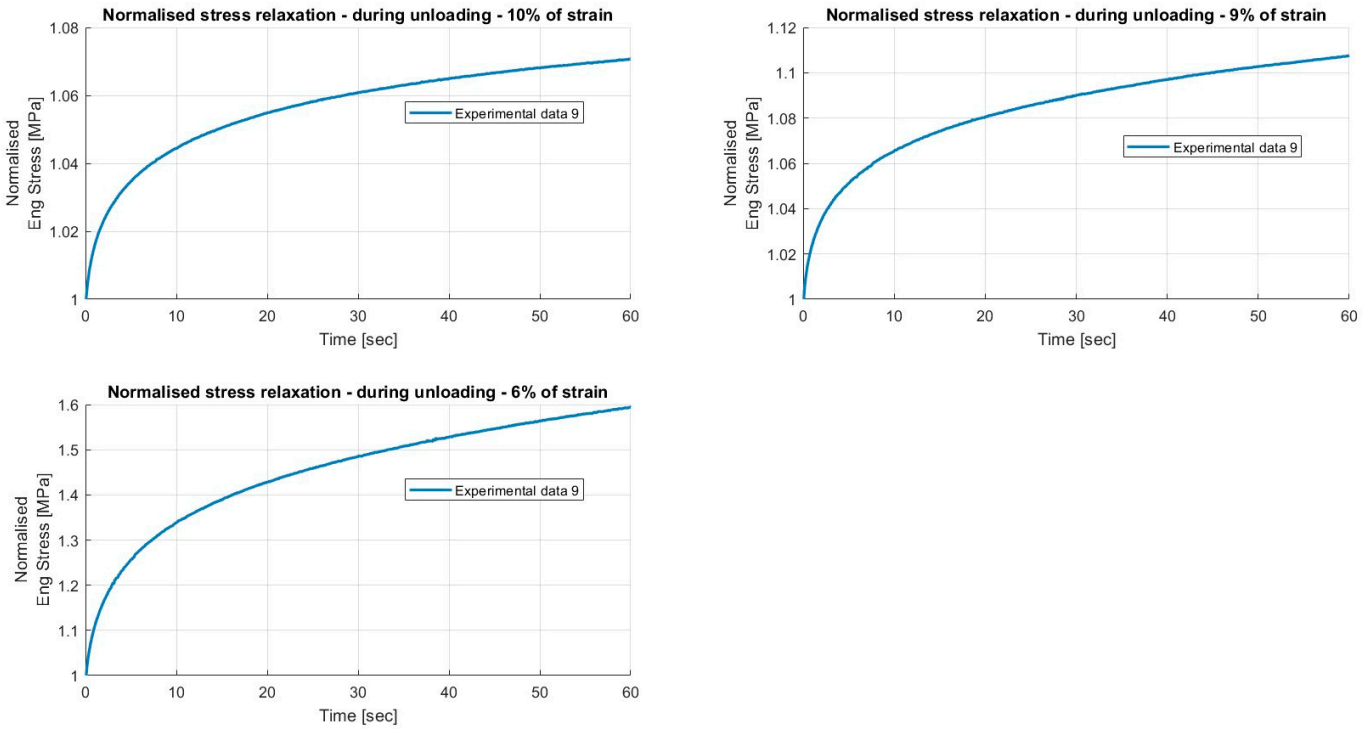

Figure 18. Results of the relaxation segments, during the unloading phase, on porcine FDS tendons classified in the "Thin" category, with a relaxation time of 60 s. In each graph, the same normalised relaxation segment for all specimens is reported.

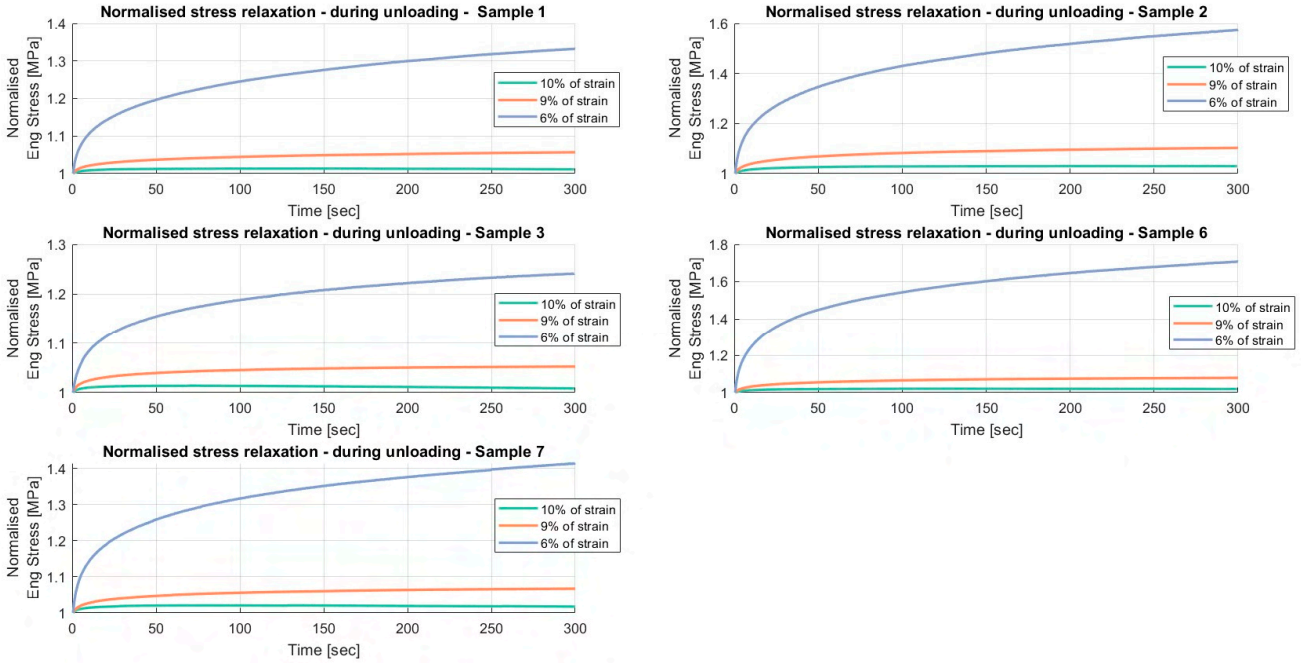

Figure 19. Results of the relaxation segments, during the unloading phase, on porcine FDS tendons classified in the "Thin" category, with a relaxation time of 300 s. In each graph, all the normalised relaxation segments for the same specimen are reported.

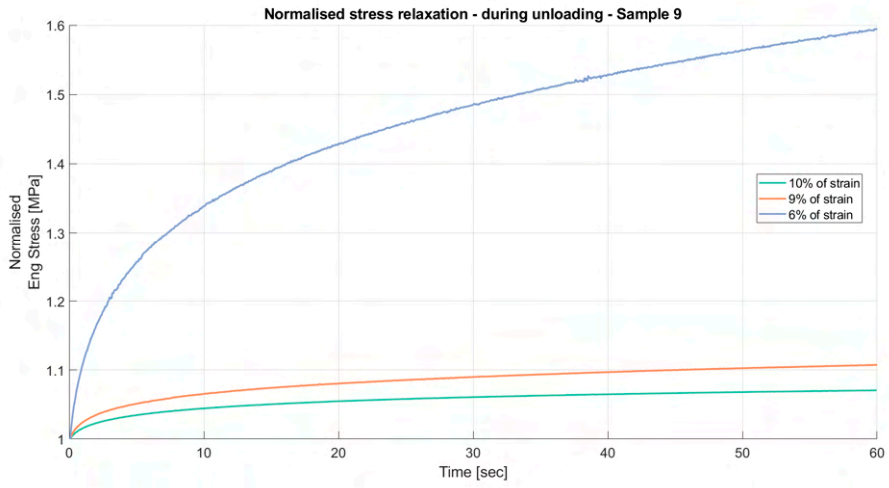

Figure 20. Results of the relaxation segments, during the unloading phase, on porcine FDS tendons classified in the "Thin" category, with a relaxation time of 60 s. In each graph, all the normalised relaxation segments for the same specimen are reported.

Figures 13 and 17 present the normalised relaxation segments during unloading with a hold time of 300 s. When no relaxation phase was introduced at 12% strain (during loading), the relaxation segments recorded at 10% strain (during unloading) exhibited an atypical response, characterised by an initial increase in normalised stress followed by a subsequent decrease. This behaviour may be associated with experimental conditions rather than representing an intrinsic material property.

Figures 14 and 18 show the normalised relaxation segments during unloading with a hold time of 60 s when an additional relaxation phase was included at 12% strain. This second experimental protocol eliminated the atypical behaviour observed in the tests performed without the relaxation phase at 12% strain (during loading), suggesting that the

phenomenon was likely related to the specific testing procedure rather than to the inherent mechanical response of the tendon tissue.

3.2. Constitutive Modelling Results

The following subsections report the constitutive model parameters obtained from the calibration (see Tables 5 and 6 for the incompressible model and Tables 7 and 8 for the nearly incompressible model).

3.2.1. Incompressible Formulation Fitting Results

The incompressible model adopted for the constitutive modelling of the FDS tendons showed good agreement with the experimental data. Although the model prediction generally decreased with increasing deformation, the calculated R^2 values remained above 0.90 for all specimens. Overall, the constitutive model obtained using the experimental data with a relaxation time of 300 s provided a better approximation of the viscous behaviour. When comparing the numerical models calibrated on experimental tests with relaxation times of 300 and 60 s, the mean R^2 value was higher for the calibration performed with a relaxation time of 300 s ("Thick" category: 0.982 versus 0.949; "Thin" category: 0.9754 versus 0.970).

Figures 21–24 compare the numerical model with experimental data using the incompressible formulation. Figures 21 and 23 illustrate the results for a 300 s hold time in the "Thick" and "Thin" categories, respectively, while Figures 22 and 24 present the corresponding results for a 60 s hold time.

Table 5. Mechanical parameters of the incompressible model for FDS tendons classified in the "Thick" category.

	Specimen 1	Specimen 2	Specimen 3	Specimen 4	Specimen 5	Specimen 6	Specimen 7	Specimen 8	Specimen 9	Specimen 10
C_1 [MPa]	9.640	5.017	0.030	0.344	9.763	3.715	0.426	0.020	1.065	0.026
α_1	0.091	0.032	5.171	0.154	0.093	0.040	0.053	9.818	0.045	2.638
C_4 [MPa]	33.773	40.751	25.991	57.699	110.076	59.197	55.539	10.358	47.722	29.925
α_4	4.642	2.868	6.340	5.567	4.336	2.313	3.345	13.621	2.634	6.776
γ_m^1	0.013	0.033	0.109	0.097	0.056	0.061	0.094	0.102	0.052	0.165
τ_m^1 [s]	0.003	0.003	0.004	0.006	0.003	0.004	0.003	0.002	0.005	0.005
γ_m^2	0.055	0.099	0.181	0.035	0.014	0.026	0.023	0.157	0.016	0.118
τ_m^2 [s]	0.028	0.026	0.058	0.018	0.038	0.039	0.020	0.026	0.029	0.044
γ_m^3	0.014	0.045	0.118	0.009	0.055	0.010	0.016	0.113	0.014	0.075
τ_m^3 [s]	0.117	0.114	0.310	0.132	0.158	0.155	0.178	0.210	0.113	0.272
γ_m^4	0.009	0.010	0.047	0.059	0.032	0.009	0.089	0.057	0.037	0.022
τ_m^4 [s]	121.697	20.956	25.922	85.193	24.406	33.094	11.290	103.297	77.115	34.822
γ_f^1	0.042	0.061	0.105	0.037	0.042	0.157	0.124	0.342	0.449	0.490
τ_f^1 [s]	0.003	0.005	0.005	0.005	0.003	0.003	0.002	0.003	0.008	0.008
γ_f^2	0.077	0.084	0.064	0.106	0.018	0.085	0.033	0.302	0.038	0.116
τ_f^2 [s]	0.028	0.020	0.023	0.020	0.033	0.018	0.013	0.024	0.015	0.027
γ_f^3	0.005	0.046	0.010	0.029	0.063	0.077	0.016	0.018	0.019	0.001
τ_f^3 [s]	0.123	0.105	0.141	0.126	9.976	9.993	0.107	0.150	9.296	0.127
γ_f^4	0.214	0.224	0.177	0.085	0.080	0.084	0.157	0.102	0.087	0.148
τ_f^4 [s]	53.770	59.478	82.160	68.213	258.209	72.025	40.922	159.306	13.503	169.095
R^2	0.959	0.988	0.985	0.991	0.992	0.978	0.982	0.907	0.979	0.961

Table 6. Mechanical parameters of the incompressible model for FDS tendons classified in the "Thin" category.

	Specimen 1	Specimen 2	Specimen 3	Specimen 4	Specimen 5	Specimen 6	Specimen 7	Specimen 8	Specimen 9	Specimen 10
C_1 [MPa]	2.775	9.967	6.669	9.567	9.939	3.962	9.939	0.070	0.019	0.049
α_1	0.084	0.015	0.033	9.904	0.007	1.519	0.126	4.857	4.123	9.795
C_4 [MPa]	118.154	41.288	75.883	110.5404	130.276	58.914	60.521	32.291	36.561	44.418
α_4	0.085	3.911	2.540	4.143	3.246	3.052	2.046	7.268	6.917	9.096
γ_m^1	0.030	0.007	0.059	0.240	0.116	0.395	0.087	0.113	0.073	0.054
τ_m^1 [s]	0.006	0.005	0.008	0.004	0.003	0.008	0.007	0.004	0.002	0.004
γ_m^2	0.025	0.040	0.019	0.125	0.046	0.257	0.034	0.053	0.149	0.104
τ_m^2 [s]	0.020	0.039	0.052	0.031	0.043	0.019	0.035	0.036	0.054	0.049
γ_m^3	0.119	0.007	0.038	0.031	0.009	0.114	0.106	0.019	0.138	0.033
τ_m^3 [s]	0.128	0.130	0.128	0.133	0.159	0.146	0.159	0.443	0.532	0.198
γ_m^4	0.022	0.003	0.012	0.310	0.101	0.221	0.007	0.023	0.026	0.055
τ_m^4 [s]	18.171	37.908	75.446	23.082	23.310	419.029	92.929	47.096	48.620	41.410
γ_f^1	0.055	0.065	0.062	0.030	0.017	0.329	0.184	0.296	0.316	0.092
τ_f^1 [s]	0.003	0.006	0.003	0.003	0.004	0.004	0.003	0.004	0.006	0.006
γ_f^2	0.042	0.042	0.026	0.014	0.012	0.148	0.304	0.092	0.110	0.043
τ_f^2 [s]	0.021	0.036	0.022	0.032	0.035	0.063	0.022	0.022	0.028	0.026
γ_f^3	0.011	0.003	0.010	0.009	0.004	0.060	0.058	0.003	0.085	0.065
τ_f^3 [s]	0.121	0.103	0.132	0.115	0.116	9.799	0.126	0.126	6.575	0.106
γ_f^4	0.158	0.191	0.198	0.074	0.109	0.025	0.161	0.303	0.114	0.268
τ_f^4 [s]	55.523	33.553	66.865	365.545	224.304	17.236	342.302	304.087	131.705	167.130
R^2	0.980	0.960	0.984	0.992	0.976	0.969	0.967	0.956	0.981	0.974

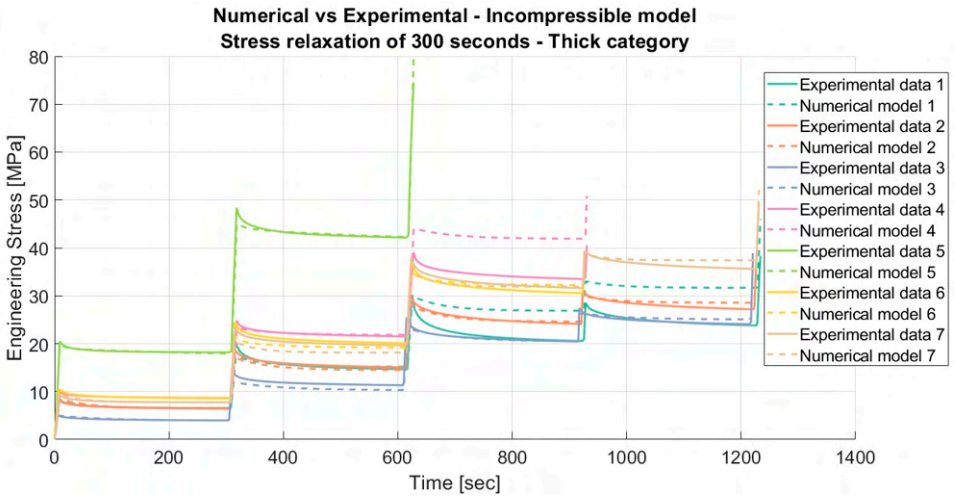

Figure 21. Results of the calibration procedure for the incompressible material model on porcine FDS tendons classified in the "Thick" category, with a relaxation time of 300 s.

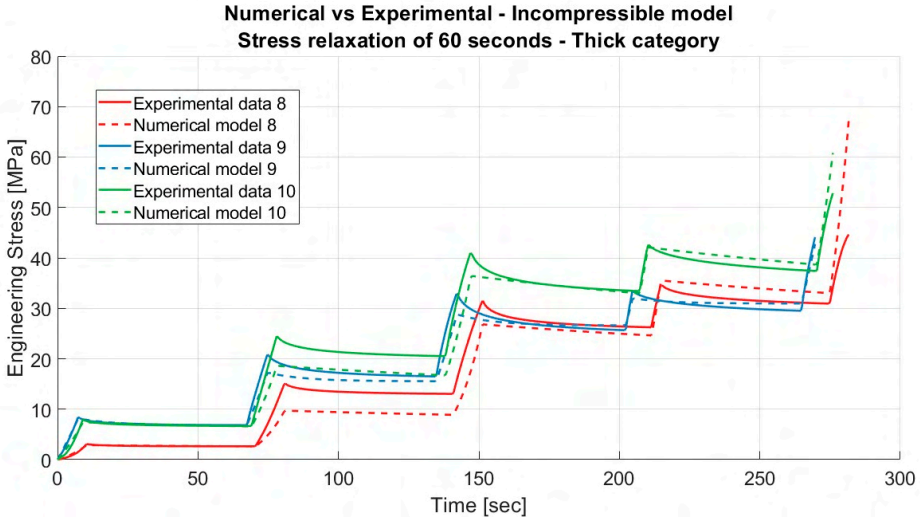

Figure 22. Results of the calibration procedure for the incompressible material model on porcine FDS tendons classified in the "Thick" category, with a relaxation time of 60 s.

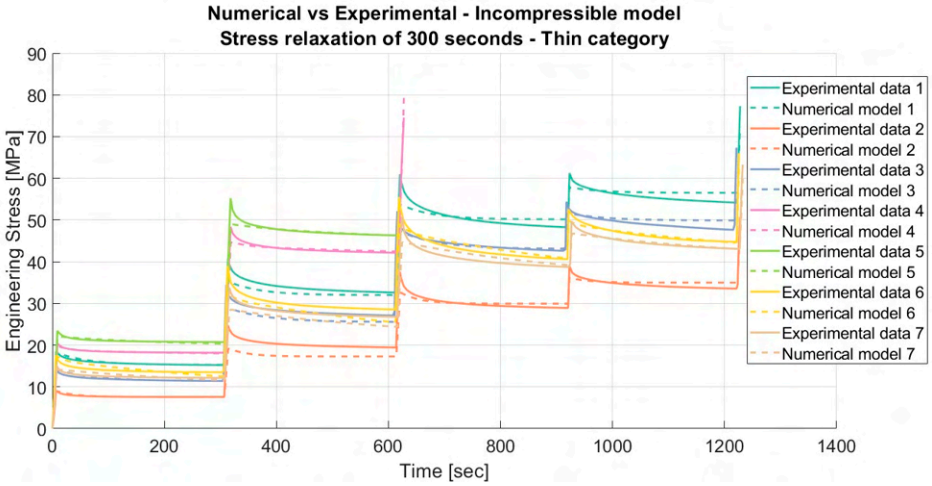

Figure 23. Results of the calibration procedure for the incompressible material model on porcine FDS tendons declassified in the "Thin" category, with a relaxation time of 300 s.

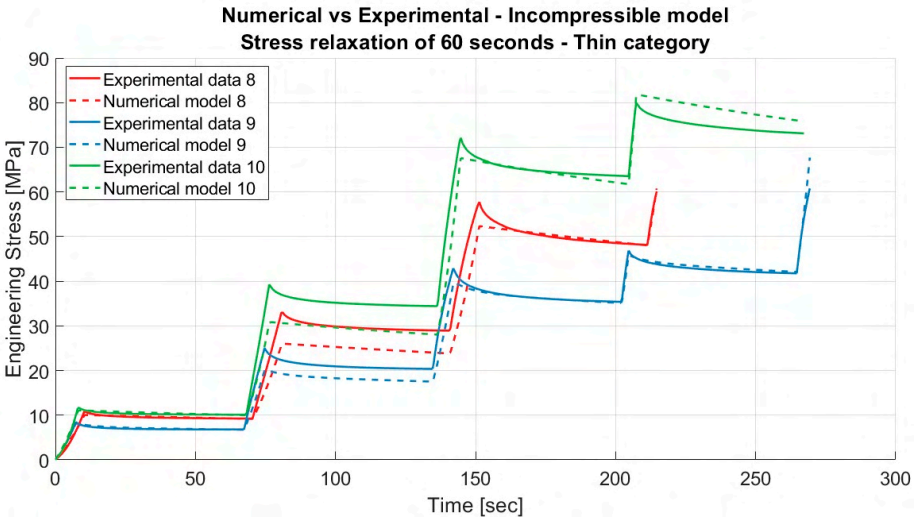

Figure 24. Results of the calibration procedure for the incompressible material model on porcine FDS tendons classified in the "Thin", with a relaxation time of 60 s.

3.2.2. Nearly Incompressible Formulation Fitting Results

The nearly incompressible model adopted for the constitutive modelling of the FDS tendons shows good agreement with the experimental data. As reported for the incompressible constitutive formulation, the model prediction generally decreased with increasing deformation. However, for this model, the calculated R^2 values for some specimens were less than 0.90.

Considering the constitutive models calibrated using experimental data with relaxation times of either 300 or 60 s, no conclusive evidence emerged that a longer relaxation period systematically improves the fitting accuracy. When comparing the numerical models obtained from the two relaxation times, the mean R^2 values were only marginally higher for the calibration performed with a relaxation time of 300 s ("Thick" category: 0.956, excluding Specimen 5, vs. 0.959; "Thin" category: 0.924, excluding Specimens 4 and 5, vs. 0.957). Nevertheless, the graphical comparison indicates that the model calibrated with a relaxation time of 300 s provides a more accurate representation of the relaxation behaviour, particularly in capturing the overall stress decay trend.

Figures 25–28 show the comparison between the numerical model and experimental data using the nearly incompressible formulation. Results for a hold time of 300 s are reported in Figures 25 and 27 for the "Thick" and "Thin" categories, whereas Figures 26 and 28 display the corresponding results for a 60 s hold time.

Table 7. Mechanical parameters of the nearly incompressible model for FDS tendons classified in the "Thick" category.

	Specimen 1	Specimen 2	Specimen 3	Specimen 4	Specimen 5	Specimen 6	Specimen 7	Specimen 8	Specimen 9	Specimen 10
C_1 [MPa]	3.718	0.0001	0.0001	9.799	10.0	9.931	0.343	0.002	0.0001	0.001
α_1	9.999	9.973	9.996	9.999	9.999	4.217	9.991	10.0	8.782	10.0
C_4 [MPa]	69.190	79.825	53.101	76.046	99.999	75.166	94.078	64.176	79.458	84.600
α_4	0.039	3.525	9.999	5.963	9.999	5.363	5.734	10.0	4.609	10.0
β_m^1	0.954	3.001	3.148	0.017	62.377	1.946	17.183	0.266	22.805	4.998
τ_m^1 [s]	0.006	0.002	0.006	0.006	0.002	0.004	0.004	0.006	0.002	0.001
β_m^2	0.001	0.251	0.001	0.004	0.008	0.010	0.014	0.001	0.035	0.002
τ_m^2 [s]	0.112	0.100	0.121	0.100	0.114	0.100	0.151	0.103	0.171	0.100
β_m^3	0.0128	0.185	0.011	0.001	0.016	0.013	0.006	0.001	0.015	0.001
τ_m^3 [s]	1.000	1.000	9.938	1.012	1.000	9.999	1.024	1.000	1.038	1.000
β_m^4	3.407	35.033	0.063	0.001	0.001	0.002	0.033	0.001	0.001	0.002
τ_m^4 [s]	43.024	21.500	23.349	57.395	10.000	15.672	14.820	10.000	15.637	99.996
β_f^1	78.566	0.251	0.055	34.956	0.0063	8.065	7.440	0.132	77.597	71.354
τ_f^1 [s]	0.001	0.010	0.070	0.004	0.008	0.002	0.004	0.005	0.001	0.001
β_f^2	0.006	0.055	0.001	0.007	0.022	0.001	0.001	0.002	0.013	0.002
τ_f^2 [s]	0.100	0.100	0.129	0.100	0.115	0.103	0.106	0.100	0.125	0.100
β_f^3	0.016	0.035	0.001	0.004	0.007	0.001	0.011	0.001	0.254	0.003
τ_f^3 [s]	9.995	10.000	9.992	1.013	1.005	10.000	9.999	1.000	9.997	1.000
β_f^4	0.001	0.251	0.063	0.122	1.712	0.269	0.175	0.001	0.001	0.001
τ_f^4 [s]	40.077	26.723	29.329	44.419	100.0	41.598	20.953	10.000	22.047	61.677
K [MPa]	9024.4	1009.0	1005.3	6176.5	1622.3	4763.1	8486.9	8543.0	1000.47	10000
R^2	0.918	0.984	0.977	0.943	0.692	0.939	0.975	0.964	0.974	0.940

Table 8. Mechanical parameters of the nearly incompressible model for FDS tendons classified in the "Thin" category.

	Specimen 1	Specimen 2	Specimen 3	Specimen 4	Specimen 5	Specimen 6	Specimen 7	Specimen 8	Specimen 9	Specimen 10
C_1 [MPa]	9.991	0.118	10.0	9.994	9.996	10.00	0.0001	9.998	0.028	9.993
α_1	8.216	9.962	10.0	9.996	9.996	7.876	9.999	10.0	9.999	9.998
C_4 [MPa]	99.997	89.318	100.0	99.999	99.996	100. 0	100.0	99.999	73.208	99.999
α_4	8.541	5.424	6.319	9.996	9.998	3.954	7.544	9.999	9.999	9.999
β_m^1	56.949	45.862	0.427	2.602	46.005	29.366	43.731	12.300	29.086	39.487
τ_m^1 [s]	0.004	0.009	0.005	0.006	0.002	0.005	0.010	0.004	0.002	0.006
β_m^2	0.001	0.251	0.004	0.030	0.037	0.005	0.001	0.003	0.033	0.005
τ_m^2 [s]	0.225	0.331	0.102	0.100	0.100	0.100	0.134	0.102	0.100	0.126
β_m^3	0.243	0.001	0.007	0.017	0.012	0.004	0.003	0.001	0.001	0.001
τ_m^3 [s]	1.038	9.966	1.000	1.017	1.000	1.003	1.008	1.000	1.000	1.029
β_m^4	1.653	12.613	0.001	0.013	0.001	0.001	20.530	0.007	0.001	0.013
τ_m^4 [s]	99.960	84.096	99.999	99.942	91.895	100.0	10.013	10.000	99.982	99.998
β_f^1	56.832	53.653	81.558	25.168	0.126	78.753	32.667	45.162	12.533	43.972
τ_f^1 [s]	0.009	0.005	0.002	0.009	0.006	0.005	0.001	0.002	0.005	0.002
β_f^2	0.063	0.047	0.001	0.029	0.030	0.004	0.001	0.001	0.015	0.015
τ_f^2 [s]	0.154	0.151	0.107	0.145	0.117	0.107	0.100	0.100	0.100	0.114
β_f^3	0.001	0.257	0.003	0.001	0.016	0.001	0.002	0.007	0.001	0.001
τ_f^3 [s]	1.060	9.980	1.000	1.012	1.000	1.000	1.006	1.007	1.012	1.020
β_f^4	0.750	0.001	0.402	1.679	1.794	0.861	0.785	0.075	0.597	0.772
τ_f^4 [s]	99.956	89.205	100.0	99.998	99.997	100.0	100.0	100.0	99.990	99.989
K [MPa]	9906.8	6939.7	1046.9	6415.1	9304.9	9680.9	1010.6	7800.9	7301.3	7455.2
R^2	0.915	0.954	0.957	0.565	0.549	0.902	0.893	0.928	0.985	0.957

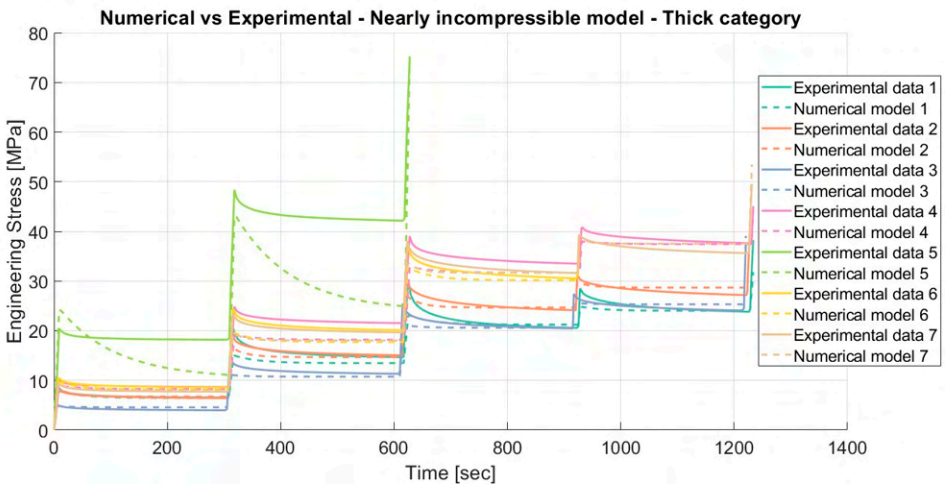

Figure 25. Results of the calibration procedure for the nearly incompressible material model on porcine FDS tendons classified in the "Thick" category, with a relaxation time of 300 s.

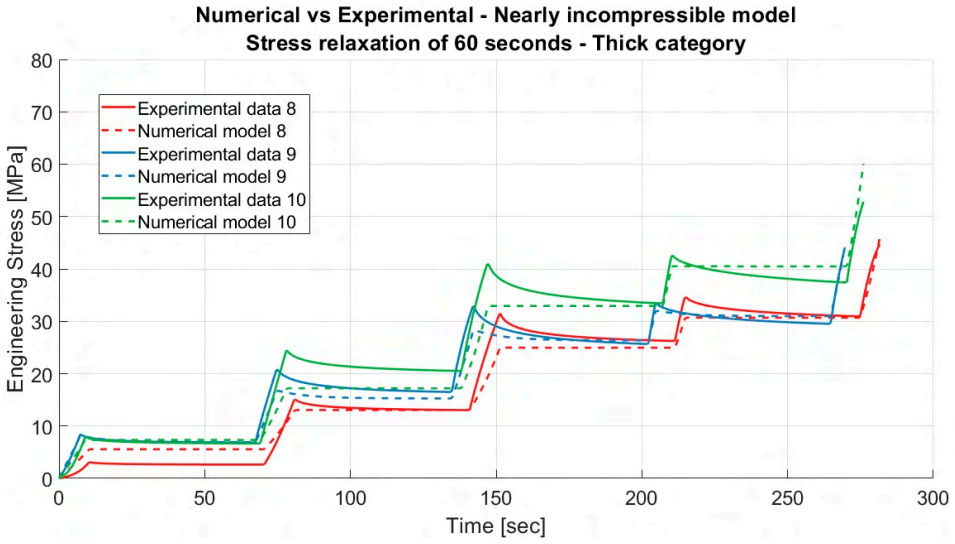

Figure 26. Results of the calibration procedure for the nearly incompressible material model on porcine FDS tendons classified in the "Thick" category, with a relaxation time of 60 s.

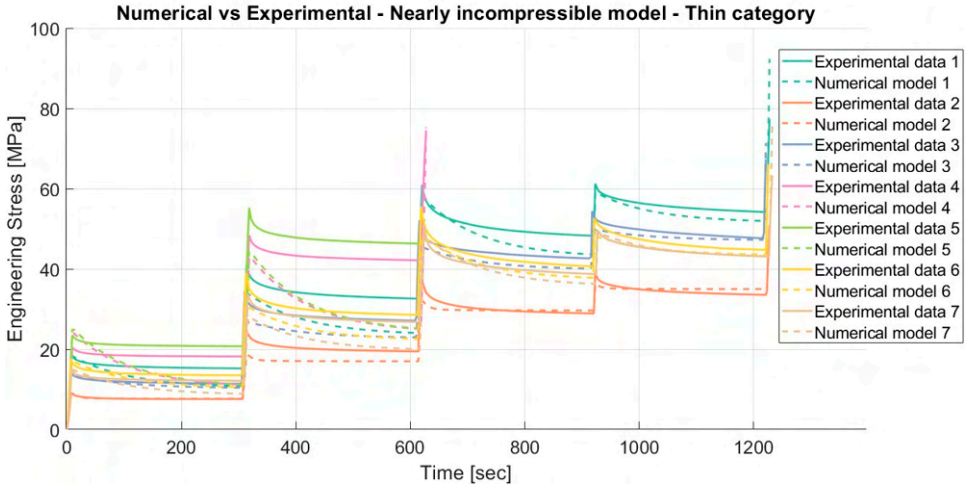

Figure 27. Results of the calibration procedure for the nearly incompressible material model on porcine FDS tendons classified in the "Thin" category, with a relaxation time of 300 s.

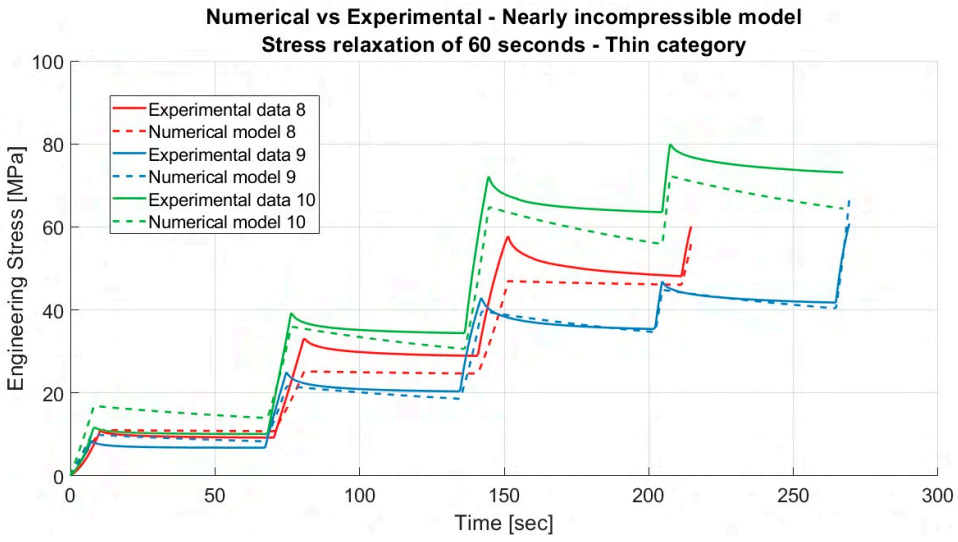

Figure 28. Results of the calibration procedure for the nearly incompressible material model on porcine FDS tendons classified in the "Thin" category, with a relaxation time of 60 s.

4. Discussion

Previous studies on the mechanical properties of animal and human tendons highlight a similarity between the range of Young's modulus of porcine FDP tendons and human hand flexor tendons [7]. This evidence is reinforced by the widespread use of porcine tendons to evaluate the performance of different suture patterns.

In this work, a detailed investigation of the mechanical properties of porcine FDS tendons was carried out using the most widely adopted experimental protocol for soft tissue characterisation. Human hand flexor tendons are extensively studied due to their susceptibility to injury and work-related musculoskeletal disorders, which impose significant societal and industrial costs. Recent studies on human FDP and FDS tendons under cyclic loading revealed a logarithmic relationship between applied stress and fatigue life, improving the accuracy of models of carpal tunnel syndrome and trigger finger [26].

Additionally, the stiffness at the FDP attachment site was found to be comparable with that of more proximal regions [27], and the role of the pulleys in tendon function has also been investigated [28].

Generally, stress-relaxation tests at different strain levels allow the viscoelastic behaviour of soft tissues to be observed. This experimental approach is well established in the literature, and various soft tissues have been investigated [29–31].

The idea of introducing relaxation segments during the unloading phase was inspired by studies on the mechanical characterisation of thermoplastic polymers [23].

The results of the experimental campaign revealed variability among specimens. Considering width and thickness measurements, statistical analysis revealed a significant difference in thickness ($p < 0.05$), with tendons in the "Thick" category exhibiting greater thickness than those in the "Thin" category. Furthermore, a significant difference in width ($p < 0.05$) was observed only at the medial and proximal sites, with greater widths in the "Thick" group.

The relaxation process is commonly analysed using a relaxation period of approximately 300 s [15]. The data collected using a relaxation time of only 60 s exhibited lower PSL values compared with those obtained with longer relaxation durations. A relaxation period of 60 s is insufficient for the viscous mechanisms to reach the plateau phase. From the perspective of constitutive modelling, a relaxation time of 300 s allows a more thorough investigation of the viscous behaviour of the soft tissues under study. In particular, the constitutive modelling provided better results in capturing the experimental behaviour when a longer relaxation period was adopted for the relaxation segments.

The PSL parameter allows quantification of the relaxation process exhibited by the tissues during the relaxation phase. An interesting observation emerged when analysing the relaxation segment at 10% strain during the loading phase: the PSL value was lower than those obtained at 3%, 6%, and 9% strain, where PSL increased with tissue strain (see Tables 2 and 3). In contrast, at 12% strain, the PSL value followed the same increasing trend observed at 3%, 6%, and 9% strain. This result remains unclear and warrants further investigation, particularly through experimental procedures adopting multiple relaxation segments at closely spaced strain levels, with differences no greater than 1% strain.

Evaluating the relaxation phases during the unloading phase, the PSL parameter exhibited an increase in value as the strain level decreased. Comparing the mean values calculated for each relaxation segment during unloading, the second methodology, in which a relaxation segment at 12% strain was included, showed an increase in relaxation (tendons in the "Thick" category: 10%—1.28 vs. 7.58; 9%—7.26 vs. 11.59; 6%—45.04 vs. 70.69; tendons in the "Thin" category: 10%—1.73 vs. 7.06; 9%—7.17 vs. 10.76; 6%—45.40 vs. 59.38; for further details, see Tables 2 and 3). However, due to the presence of unusual

behaviour in the tests performed with the first experimental protocol, the unloading phase is not considered reliable.

Considering the PSL values computed during loading and unloading, a statistical comparison of PSL values between the two groups revealed no significant differences ($p > 0.05$), indicating that the grouping does not influence the interpretation of the viscous behaviour. However, for the PSL values during unloading in the second experimental protocol, the limited number of specimens in the "Thin" category did not allow a t-test to be performed.

Furthermore, the unusual behaviour observed during the relaxation segment at 10% strain (unloading) was evident only in the experimental data obtained without the inclusion of a relaxation segment at 12% strain. Therefore, this atypical response of the tendon specimens could be attributed to the experimental protocol adopted.

After identifying this unusual behaviour, the equipment was carefully checked, and no evidence of any problem was found.

For future tests, the second methodology, in which an additional relaxation segment is included at 12% strain, will be adopted. Further experiments are required to determine whether this unusual behaviour is indeed related to the experimental protocol. The preliminary results of this study suggest that the observed behaviour arises from the absence of the relaxation segment at 12% strain. The issue might be attributed to the inversion of the movement direction of the traction machine, even though a brief holding time of 1 s was used to perform the direction reversal in the protocols.

Due to the presence of the unusual behaviour, the calibration of the constitutive models was performed considering only the loading portion of the tests. Including the unloading behaviour in future tests could further enhance the accuracy of the calibration.

Provenzano et al. (2001) [32] reported a decrease in the rate of relaxation during stress-relaxation tests on ligaments at different strain levels [29]. Furthermore, they observed that the rate of creep depends on the load level, while the rate of relaxation depends on the strain level [32].

Considering Figures 7 and 11, increasing the strain caused both FDS tendons to show a reduction in relaxation, as reflected by the PSL calculations. In contrast, Figures 8 and 12, which include a stress-relaxation segment at 12% strain, reveal that increasing the strain beyond 10% resulted in greater relaxation, consistent with the PSL calculations.

The increase in relaxation observed beyond 10% strain remains unclear. This behaviour is likely associated with the onset of inelastic effects, potentially resulting from testing the specimens beyond their physiological loading regime.

The constitutive modelling of the FDS tendons, using both incompressible and nearly incompressible formulations, showed good agreement with the experimental data. Both formulations yielded satisfactory R^2 values. The incompressible formulation provided R^2 values greater than 0.90.

By contrast, the nearly incompressible formulation produced some calibrations with lower R^2 values: 0.692 for Specimen 5 of the "Thick" category, and 0.565 and 0.549 for Specimens 4 and 5 of the "Thin" category. However, the other calibrations also yielded R^2 values greater than 0.90. It is important to note that the boundary search range in the GA for material parameter calibration was kept fixed; adopting a specimen-specific boundary range for each specimen could potentially lead to improved results. For example, specimen 5 of the "Thick" category exhibited a stiffer behaviour compared with other specimens in the same category. Similarly, Specimens 4 and 5 of the "Thin" category showed stiffer behaviour compared with the other specimens in that category.

Considering the entire experimental test, which involved stress-relaxation during both the loading and unloading phases, the constitutive models were less accurate in capturing the mechanical behaviour during the unloading phase.

Figures 29–32 present the comparison between the experimental data and the numerical predictions obtained using the incompressible formulation. By contrast, Figures 33–36 show the comparison between the experimental data and the numerical predictions obtained using the nearly incompressible formulation.

By evaluating the constitutive model parameters obtained during calibration, it is possible to observe a considerable variability in the values. The visco-hyperelastic model, based on the assumption of incompressible material, includes 20 parameters. Instead, the visco-hyperelastic model, based on the assumption of nearly incompressible material, includes 21 parameters.

Part of this variability is due to differences between specimens. However, another part is inherent to the number of model parameters, as multiple combinations of parameters can lead to similarly good results. Adopting different experimental tests with other loading conditions could help reduce the variability in the model parameter values.

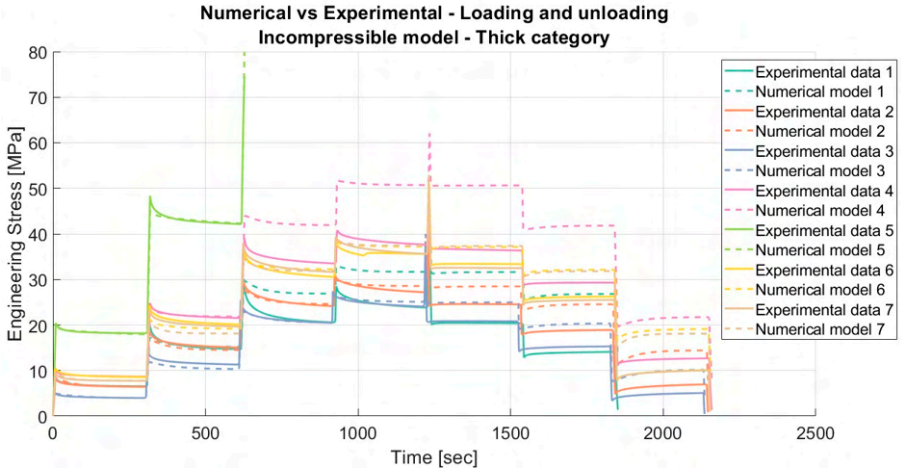

Figure 29. Results for the incompressible material model applied to porcine FDS tendons of the "Thick" category for loading and unloading, with a relaxation time of 300 s.

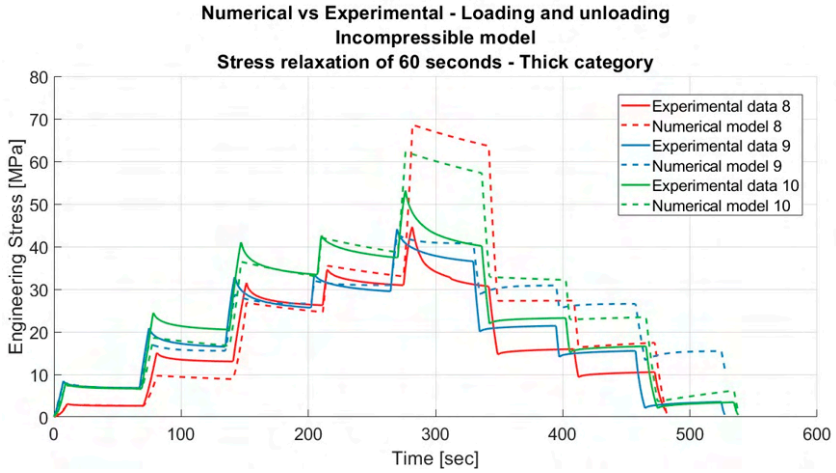

Figure 30. Results for the incompressible material model applied to porcine FDS tendons of the "Thick" category for loading and unloading, with a relaxation time of 60 s.

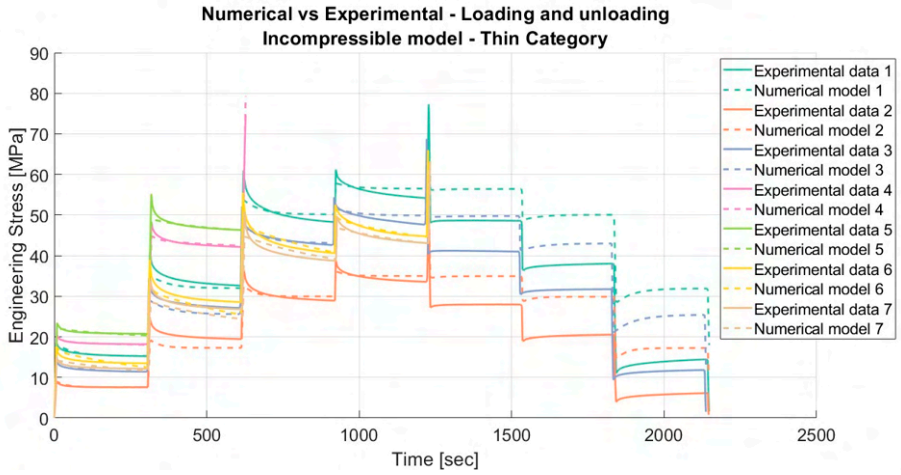

Figure 31. Results for the incompressible material model applied to porcine FDS tendons of the "Thin" category for loading and unloading, with a relaxation time of 300 s.

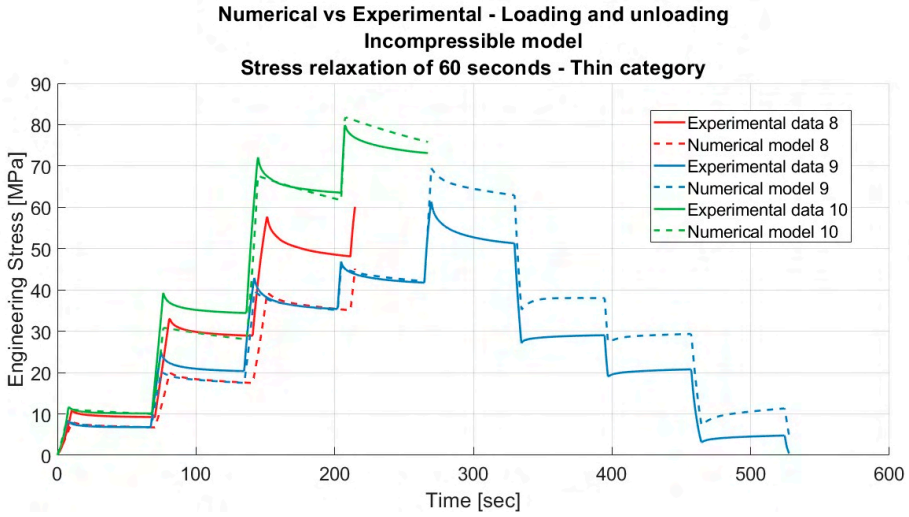

Figure 32. Results for the incompressible material model applied to porcine FDS tendons of the "Thin" category for loading and unloading, with a relaxation time of 60 s.

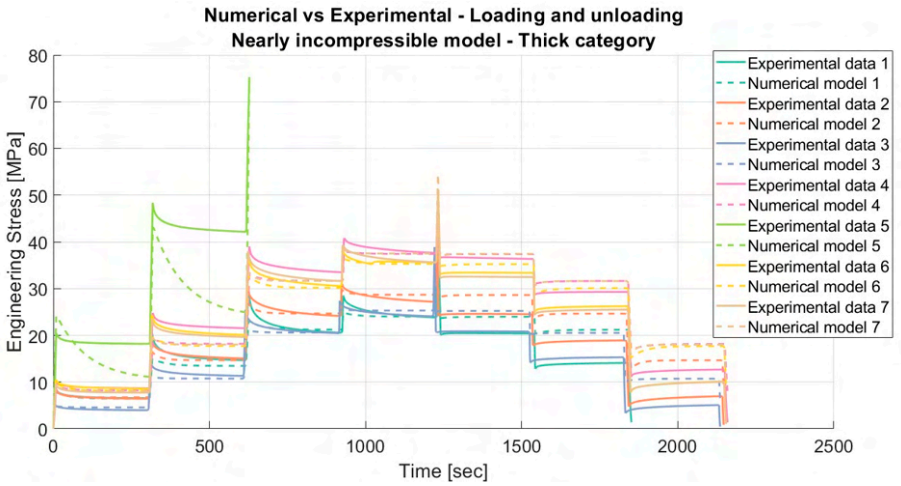

Figure 33. Results for the nearly incompressible material model applied to porcine FDS tendons of the "Thick" category for loading and unloading, with a relaxation time of 300 s.

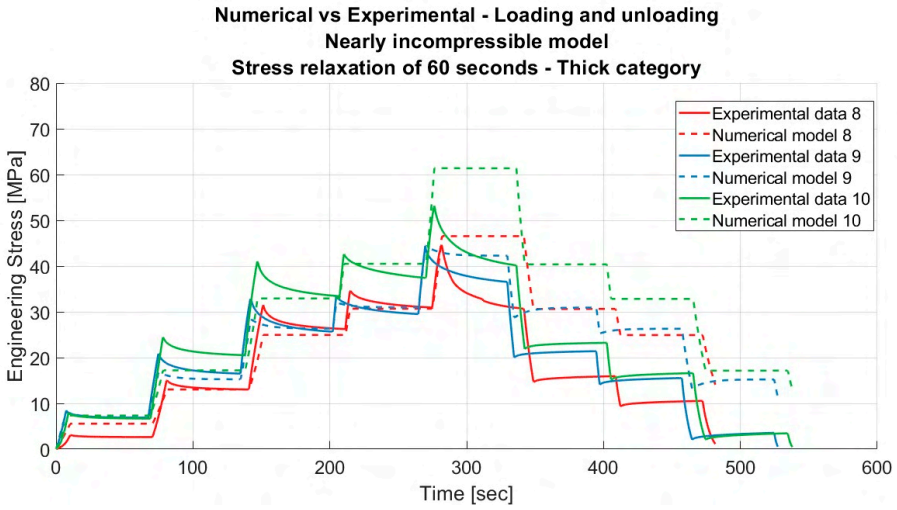

Figure 34. Results for the nearly incompressible material model applied to porcine FDS tendons of the "Thick" category for loading and unloading, with a relaxation time of 60 s.

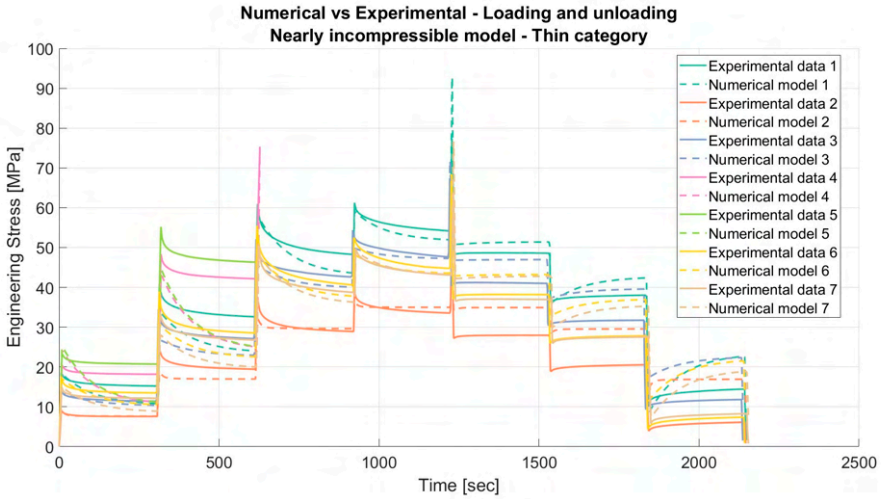

Figure 35. Results for the nearly incompressible material model applied to porcine FDS tendons of the "Thin" category for loading and unloading, with a relaxation time of 300 s.

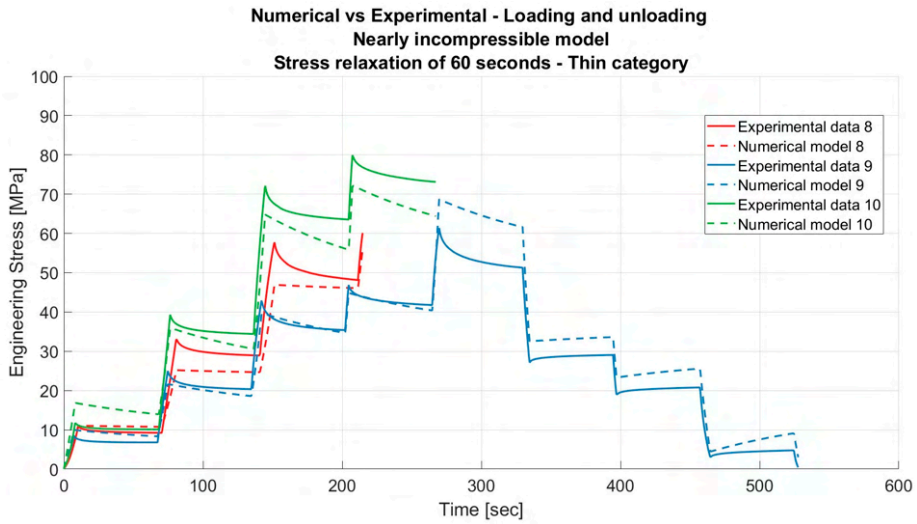

Figure 36. Results for the nearly incompressible material model applied to porcine FDS tendons of the "Thin" category for loading and unloading, with a relaxation time of 60 s.

To limit the variability of the material model parameters, in the GA, the values for each parameter were constrained by adopting the same range for all specimens. Further efforts should consider adopting constitutive formulations with a lower number of material parameters.

Based on the results obtained in this work, it is not possible to determine average model parameters due to the considerable variability. Each combination obtained represents a patient-specific model.

Considering the performance of the constitutive models adopted, the predictive accuracy generally decreases at higher strain levels. The reduction in accuracy for both models could be attributed to their limitation in using linear viscous terms to represent the viscous behaviour of soft tissues. Both models are extensions of the classical Boltzmann superposition principle to finite strain, in which the material response is assumed to be the sum of a strain rate-independent and a strain rate-dependent component. The strain rate dependency is modelled through a time convolution integral [33,34].

However, soft tissues exhibit complex time- and rate-dependent material properties [35,36]. Previous studies have shown that the influence of strain level on relaxation phenomena can be interpreted by linear viscous terms when specific conditions are satisfied [15]. The accuracy of both models could be improved by adding additional linear viscous terms or by adopting a viscoelastic model that accounts for the nonlinearity of the viscous behaviour.

The accuracy of these constitutive models could be further enhanced by incorporating additional terms that capture microstructural features. For example, the effects of collagen cross-links at the microscale, which account for softening and failure mechanisms [22].

In the literature, constitutive formulations have been reported in which the presence of a single fibre family is modelled using a continuum approach with distributed collagen orientations, capable of simulating the mechanical behaviour of tendons [21,37].

Typically, the strain energy function Ψ accounts for collagen fibre uncrimping as a mechanism for tissue nonlinearity and also includes the contribution of the isotropic matrix to the overall mechanical behaviour. Fibre–matrix interactions have not typically been included; only a few studies have evaluated and developed constitutive formulations to capture this effect [38].

However, the mechanical behaviour of soft tissues is not solely governed by the isotropic matrix and fibre stretch, but is also influenced by fibre–matrix interactions. Indeed, the literature reports that material behaviour arises from matrix properties, fibre–matrix interactions, and fibre–fibre interactions [39].

Fibre–matrix interactions are commonly evaluated through simple shear tests, and different constitutive formulations have been proposed for this contribution [40,41]. Nevertheless, the evaluation of fibre–matrix interactions has mainly focused on the anulus fibrosus. The constitutive modelling of fibre–matrix interactions in tendon mechanics represents a key aspect that requires further investigation. A deeper understanding of these interactions could provide valuable insights into the failure mechanisms of suture patterns and support the development of improved tendon repair devices and techniques.

In a finite element model involving both the tendon and the muscle to which it is attached, the tendon could be modelled using the passive constitutive laws presented here, while a different constitutive model describing active behaviour, could be applied to the muscle [42].

Generally, the numerical simulation of common materials relies on a single-field variational principle. However, this approach is not appropriate for the analysis of nearly incompressible or incompressible materials, such as the soft tissues reported in this article, because it is associated with a locking effect that leads to element stiffening. For the

numerical simulation of soft tissues, the mixed Jacobian pressure formulation, derived from a three-field Hu–Washizu variational principle, represents the most effective approach to address this numerical challenge [18,25].

However, further tests are required to determine whether the calibrated models accurately represent the visco-hyperelastic response of the tissue. The calibration presented in this study effectively captures the mechanical behaviour of porcine FDS tendons along the fibre direction, which corresponds to the primary loading direction during physiological activity. Additional experimental validation is needed, particularly to investigate the mechanical response perpendicular to the fibre orientation, in order to accurately assess the matrix contribution, or to examine the viscous response of the tissue through cyclic loading and unloading, evaluating the hysteresis.

Furthermore, biaxial and shear tests should be considered to provide a more comprehensive characterisation of the tendon's mechanical behaviour. However, tendons are predominantly subjected to uniaxial tensile loads during physiological function, so uniaxial tensile testing closely reflects their in vivo mechanical environment.

5. Conclusions

This work was motivated by the need to evaluate a surrogate for human hand flexor tendons. Porcine FDP tendons have been reported in the literature as the most commonly adopted surrogate for human hand flexor tendons. In this context, porcine FDS tendons were tested using the most widely adopted experimental protocol reported in the literature.

This article presents the experimental data and evaluates the use of constitutive models based on the assumptions of incompressible and nearly incompressible materials. Both constitutive formulations accurately simulate the mechanical behaviour of FDS tendons.

The study was designed to provide an in-depth characterisation of the mechanical behaviour of porcine FDS tendons, with direct translational relevance to clinical practice. Given the increasing role of simulation in the development and evaluation of medical devices, this work offers both experimental data and numerical models that can be used to assess devices or suture techniques for hand tendon repair.

The findings could support clinicians in selecting the most appropriate suture technique for hand tendon repair and improve pre-operative planning. By developing a digital twin of the repaired tendon and integrating different suture patterns and loading conditions, valuable insights can be obtained regarding the mechanical response of the repaired tissue. The experimental data presented here provide a foundation for further numerical modelling. Based on these results, models of pathological tendons, age-related tendon degeneration, or tendon healing processes can be developed.

The adoption of a digital twin framework could allow the evaluation of stresses at the tendon–suture interface and enable prediction of the mechanical performance of various suture configurations. Ultimately, this approach may facilitate patient-specific surgical decision-making and contribute to the personalisation of rehabilitation protocols.

In the context of the T-REMEDIE project, the next step involves the creation and validation of a digital twin of FDS tendons repaired with the T-REMEDIE device for hand tendon repair.

Author Contributions: V.B.: Writing—original draft, Visualisation, Methodology, Investigation, Formal analysis, Data curation, Conceptualization. M.D.G.: Writing—original draft, Visualisation, Methodology, Investigation, Formal analysis, Data curation. P.A.: Review and editing, Validation, Supervision, Visualisation, Methodology. C.S.: Review and editing, Validation, Supervision, Resources, Project administration, Methodology, Funding acquisition. All authors have read and agreed to the published version of the manuscript.

Funding: This research received funding from EUREKA! venture SGR spa to develop the T-REMEDIE (Tendon REpair MEdical DevIcE) device for Achilles and hand tendons.

Institutional Review Board Statement: Not applicable.

Informed Consent Statement: Not applicable.

Data Availability Statement: The original contributions presented in this study are included in the article. Further inquiries can be directed to the corresponding author.

Acknowledgments: We would like to acknowledge EUREKA! venture SGR spa for supporting the project T-REM3DIE (Tendon REpair MEdical DevIcE).

Conflicts of Interest: The authors declare that this study received funding from EUREKA! Venture SGR spa. The funder was not involved in the study design, collection, analysis, interpretation of data, the writing of this article or the decision to submit it for publication.

Abbreviations

The following abbreviations are used in this manuscript:

AT	Achilles Tendon
FDP	Flexor Digitorum Profundus
FDS	Flexor Digitorum Superficialis
T-REMEDIE	Tendon Repair MEdical DevIcE
PSL	Percentage of Stress Lost

References

1. Bergamin, F.; Civera, M.; Rodriguez Reinoso, M.; Burgio, V.; Ruiz, O.G.; Surace, C. Worldwide Incidence and Surgical Costs of Tendon Injuries: A Systematic Review and Meta-Analysis. *Muscle Ligaments Tendons J.* **2023**, *13*, 31. [CrossRef]
2. Longo, U.; Salvatore, G.; Risi Ambrogioni, L.; Cella, E.; Candela, V.; Carnevale, A.; Schena, E.; Ciccozzi, M.; Maffulli, N.; Denaro, V. Epidemiology of Achilles Tendon Surgery in Italy: A Nationwide Registry Study, from 2001 through 2015. *BMC Musculoskelet. Disord.* **2020**, *21*, 687. [CrossRef]
3. de Jong, J.P.; Nguyen, J.T.; Sonnema, A.J.M.; Nguyen, E.C.; Amadio, P.C.; Moran, S.L. The Incidence of Acute Traumatic Tendon Injuries in the Hand and Wrist: A 10-Year Population-Based Study. *Clin. Orthop. Surg.* **2014**, *6*, 196–202. [CrossRef]
4. Tuncali, D.; Yavuz, N.; Terzioglu, A.; Asian, G. The Rate of Upper-Extremity Deep-Structure Injuries through Small Penetrating Lacerations. *Ann. Plast. Surg.* **2005**, *55*, 146–148. [CrossRef] [PubMed]
5. Manley, O.W.G.; Wormald, J.C.R.; Furniss, D. The Changing Shape of Hand Trauma: An Analysis of Hospital Episode Statistics in England. *J. Hand Surg. Eur. Vol.* **2019**, *44*, 532–536. [CrossRef] [PubMed]
6. Burgio, V.; Casari, S.; Milizia, M.; Sanna, F.; Spezia, G.; Civera, M.; Rodriguez Reinoso, M.; Bertuglia, A.; Surace, C. Mechanical Properties of Animal Ligaments: A Review and Comparative Study for the Identification of the Most Suitable Human Ligament Surrogates. *Biomech. Model. Mechanobiol.* **2023**, *22*, 1645–1683. [CrossRef] [PubMed]
7. Burgio, V.; Civera, M.; Reinoso, M.R.; Pizzolante, E.; Prezioso, S.; Bertuglia, A.; Surace, C. Mechanical Properties of Animal Tendons: A Review and Comparative Study for the Identification of the Most Suitable Human Tendon Surrogates. *Processes* **2022**, *10*, 485. [CrossRef]
8. Zhang, G.; Zhou, X.; Hu, S.; Jin, Y.; Qiu, Z. Large Animal Models for the Study of Tendinopathy. *Front. Cell Dev. Biol.* **2022**, *10*, 1031638. [CrossRef]
9. Bottagisio, M.; Lovati, A.B. A Review on Animal Models and Treatments for the Reconstruction of Achilles and Flexor Tendons. *J. Mater. Sci. Mater. Med.* **2017**, *28*, 45. [CrossRef]
10. Joyce, C.W.; Whately, K.E.; Chan, J.C.; Murphy, M.; O'Brien, F.J.; Carroll, S.M. Flexor Tendon Repair: A Comparative Study between a Knotless Barbed Suture Repair and a Traditional Four-Strand Monofilament Suture Repair. *J. Hand Surg. Eur. Vol.* **2014**, *39*, 40–45. [CrossRef]
11. Mao, W.F.; Wu, Y.F.; Zhou, Y.L.; Tang, J.B. A Study of the Anatomy and Repair Strengths of Porcine Flexor and Extensor Tendons: Are They Appropriate Experimental Models? *J. Hand Surg. Eur. Vol.* **2011**, *36*, 663–669. [CrossRef]
12. Havulinna, J.; Leppänen, O.V.; Järvinen, T.L.N.; Göransson, H. Comparison of Modified Kessler Tendon Suture at Different Levels in the Human Flexor Digitorum Profundus Tendon and Porcine Flexors and Porcine Extensors: An Experimental Biomechanical Study. *J. Hand Surg. Eur. Vol.* **2011**, *36*, 670–676. [CrossRef]
13. Berardo, A.; Polese, L.; Carniel, E.L.; Toniolo, I. How Does Sutures Pattern Influence Stomach Motility after Endoscopic Sleeve Gastroplasty? A Computational Study. *Updates Surg.* **2024**, *76*, 2833–2839. [CrossRef]
14. Fontanella, C.G.; Salmaso, C.; Toniolo, I.; de Cesare, N.; Rubini, A.; De Benedictis, G.M.; Carniel, E.L. Computational Models for the Mechanical Investigation of Stomach Tissues and Structure. *Ann. Biomed. Eng.* **2019**, *47*, 1237–1249. [CrossRef]
15. Carniel, E.L.; Fontanella, C.G.; Stefanini, C.; Natali, A.N. A Procedure for the Computational Investigation of Stress-Relaxation Phenomena. *Mech. Time Depend. Mater.* **2013**, *17*, 25–38. [CrossRef]
16. Berardo, A.; Bonaldi, L.; Stecco, C.; Fontanella, C.G. Biomechanical Properties of the Human Superficial Fascia: Site-Specific Variability and Anisotropy of Abdominal and Thoracic Regions. *J. Mech. Behav. Biomed. Mater.* **2024**, *157*, 106637. [CrossRef]
17. Łagan, S.D.; Liber-Kneć, A. Stress Relaxation of Porcine Tendon under Simulated Biological Environment: Experiment and Modeling. *Acta Bioeng. Biomech.* **2021**, *23*, 59–68. [CrossRef]
18. Holzapfel, G.A. Nonlinear Solid Mechanics: A Continuum Approach for Engineering Science. *Meccanica* **2002**, *37*, 489–490. [CrossRef]
19. Holzapfel, G.A.; Ogden, R.W. Constitutive Modelling of Passive Myocardium: A Structurally Based Framework for Material Characterization. *Philos. Trans. R. Soc. A Math. Phys. Eng. Sci.* **2009**, *367*, 3445–3475. [CrossRef]
20. Natali, A.N.; Carniel, E.L.; Gregersen, H. Biomechanical Behaviour of Oesophageal Tissues: Material and Structural Configuration, Experimental Data and Constitutive Analysis. *Med. Eng. Phys.* **2009**, *31*, 1056–1062. [CrossRef]

21. Sopakayang, R.; Holzapfel, G.A. A Constitutive Model of Ligaments and Tendons Accounting for Fiber-Matrix Interaction. *Int. J. Biol. Biomed. Eng.* **2017**, *11*, 245–249.
22. Holzapfel, G.A.; Ogden, R.W. A Damage Model for Collagen Fibres with an Application to Collagenous Soft Tissues. *Proc. R. Soc. A Math. Phys. Eng. Sci.* **2020**, *476*, 20190821. [CrossRef]
23. Bergstrom, J.S. *Mechanics of Solid Polymers: Theory and Computational Modeling*; William Andrew: Norwich, NY, USA, 2015; ISBN 9780323266987.
24. Holzapfel, G.A.; Gasser, T.C.; Ogden, R.W. A New Constitutive Framework for Arterial Wall Mechanics and a Comparative Study of Material Models. *J. Elast.* **2000**, *61*, 1–48. [CrossRef]
25. Holzapfel, G.A.; Gasser, T.C.; Stadler, M. A Structural Model for the Viscoelastic Behavior of Arterial Walls: Continuum Formulation and Finite Element Analysis. *Eur. J. Mech.-A/Solids* **2002**, *21*, 441–463. [CrossRef]
26. Firminger, C.R.; Smith, N.C.; Edwards, W.B.; Gallagher, S. In Vitro Fatigue of Human Flexor Digitorum Tendons. *J. Mech. Behav. Biomed. Mater.* **2025**, *163*, 106842. [CrossRef]
27. Felder, J.J.; Guseila, L.M.; Saranathan, A.; Shary, T.J.; Lippitt, S.B.; Elias, J.J. Mechanical Properties of the Flexor Digitorum Profundus Tendon Attachment. *J. Hand Microsurg.* **2013**, *5*, 54–57. [CrossRef]
28. Hamman, J.; Ali, A.; Phillips, C.; Cunningham, B.; Mass, D.P. A Biomechanical Study of the Flexor Digitorum Superficialis: Effects of Digital Pulley Excision and Loss of the Flexor Digitorum Profundus. *J. Hand Surg. Am.* **1997**, *22*, 328–335. [CrossRef]
29. Pettenuzzo, S.; Belluzzi, E.; Pozzuoli, A.; Macchi, V.; Porzionato, A.; Boscolo-Berto, R.; Ruggieri, P.; Berardo, A.; Carniel, E.L.; Fontanella, C.G. Mechanical Behaviour of Plantar Adipose Tissue: From Experimental Tests to Constitutive Analysis. *Bioengineering* **2024**, *11*, 42. [CrossRef]
30. Kainz, M.P.; Greiner, A.; Hinrichsen, J.; Kolb, D.; Comellas, E.; Steinmann, P.; Budday, S.; Terzano, M.; Holzapfel, G.A. Poro-Viscoelastic Material Parameter Identification of Brain Tissue-Mimicking Hydrogels. *Front. Bioeng. Biotechnol.* **2023**, *11*, 1143304. [CrossRef]
31. Bonaldi, L.; Berardo, A.; Pirri, C.; Stecco, C.; Carniel, E.L.; Fontanella, C.G. Mechanical Characterization of Human Fascia Lata: Uniaxial Tensile Tests from Fresh-Frozen Cadaver Samples and Constitutive Modelling. *Bioengineering* **2023**, *10*, 226. [CrossRef]
32. Provenzano, P.; Lakes, R.; Keenan, T.; Vanderby, R. Nonlinear Ligament Viscoelasticity. *Ann. Biomed. Eng.* **2001**, *29*, 908–914. [CrossRef]
33. Panda, S.K.; Buist, M.L. A Finite Nonlinear Hyper-Viscoelastic Model for Soft Biological Tissues. *J. Biomech.* **2018**, *69*, 121–128. [CrossRef]
34. Panda, S.K.; Buist, M.L. A Viscoelastic Framework for Inflation Testing of Gastrointestinal Tissue. *J. Mech. Behav. Biomed. Mater.* **2020**, *103*, 103569. [CrossRef]
35. Panda, S.K.; Buist, M.L. A Finite Element Approach for Gastrointestinal Tissue Mechanics. *Int. J. Numer. Method. Biomed. Eng.* **2019**, *35*, e3269. [CrossRef]
36. Sharma, S.; Buist, M.L. Comparing Finite Viscoelastic Constitutive Relations and Variational Principles in Modeling Gastrointestinal Soft Tissue Deformation. *J. Mech. Behav. Biomed. Mater.* **2024**, *155*, 106560. [CrossRef]
37. Bajuri, M.N.; Isaksson, H.; Eliasson, P.; Thompson, M.S. A Hyperelastic Fibre-Reinforced Continuum Model of Healing Tendons with Distributed Collagen Fibre Orientations. *Biomech. Model. Mechanobiol.* **2016**, *15*, 1457–1466. [CrossRef]
38. Klisch, S.M.; Lotz, J.C. Application of a Fiber-Reinforced Continuum Theory to Multiple Deformations of the Annulus Fibrosus. *J. Biomech.* **1999**, *32*, 1027–1036. [CrossRef]
39. Weiss, J.A.; Gardiner, J.C.; Bonifasi-Lista, C. Ligament Material Behavior Is Nonlinear, Viscoelastic and Rate-Independent under Shear Loading. *J. Biomech.* **2002**, *35*, 943–950. [CrossRef]
40. Peng, X.Q.; Guo, Z.Y.; Moran, B. An Anisotropic Hyperelastic Constitutive Model with Fiber-Matrix Shear Interaction for the Human Annulus Fibrosus. *J. Appl. Mech.* **2006**, *73*, 815–824. [CrossRef]
41. Wagner, D.R.; Lotz, J.C. Theoretical Model and Experimental Results for the Nonlinear Elastic Behavior of Human Annulus Fibrosus. *J. Orthop. Res.* **2004**, *22*, 901–909. [CrossRef]
42. Xiao, Z.; Li, C.; Wang, X.; Guo, J.; Tian, Q. Muscle Strength Identification Based on Isokinetic Testing and Spine Musculoskeletal Modeling. *Cyborg Bionic Syst.* **2024**, *2024*, 0113. [CrossRef] [PubMed]